Applied Radiation and Isotopes 236 (2026) 112727

Contents lists available at ScienceDirect

Applied Radiation and Isotopes

journal homepage: www.elsevier.com/locate/apradiso

Cross-section measurements of lanthanum radioisotopes towards an optimized production of ^{133}La and ^{135}La for theranostic applications

Gaia Dellepiane [a,b,*], Lars Eggimann [b], Alexander Gottstein [b], Samuel Juillerat [b], Eva Kasanda [b], Isidre Mateu [b], Paola Scampoli [b,c], Saverio Braccini [b]

[a] Tera-Care Foundation, Chemin du Coq-d'Inde 8a, CH-1223 Cologny, Switzerland
[b] Albert Einstein Center for Fundamental Physics (AEC), Laboratory for High Energy Physics (LHEP), University of Bern, Sidlerstrasse 5, CH-3012 Bern, Switzerland
[c] Department of Physics "Ettore Pancini", University of Napoli Federico II, Complesso Universitario di Monte S. Angelo, 80126 Napoli, Italy

ARTICLE INFO

Keywords:
Cross-section measurements
Radioisotope production
Medical cyclotrons
Lanthanum radioisotopes
Theranostics
Nuclear medicine

ABSTRACT

The theranostic pair ^{133}La/^{135}La has recently attracted growing interest as a promising candidate for combined diagnostic and therapeutic applications, owing to the favorable nuclear and chemical properties of lanthanum. ^{135}La ($t_{1/2}$ = 18.91 h) decays by electron capture (EC) to the ground state of ^{135}Ba, emitting Auger cascade electrons that are potentially useful for targeted internal radiotherapy. In contrast, ^{133}La ($t_{1/2}$ = 3.912 h) is a β^+-emitter suitable for PET imaging. Moreover, ^{133}La has been proposed as a diagnostic partner for ^{225}Ac ($t_{1/2}$ = 9.9 d), due to their close chemical similarity and the longer half-life of ^{133}La compared with other PET radiometals such as ^{68}Ga ($t_{1/2}$ = 1.13 h). A feasible approach for producing ^{133}La and ^{135}La is the irradiation of enriched ^{134}Ba and ^{135}Ba targets, respectively, with low- to medium-energy proton beams (up to 25 MeV maximum energy) readily available from medical cyclotrons. Although these production routes have been previously explored, the available nuclear data on lanthanum radioisotopes remain limited and often inconsistent. In this work, we measured the cross sections of reactions producing lanthanum isotopes up to 18 MeV, using natural $BaCO_3$ as well as enriched $^{134}BaCO_3$ and $^{135}BaCO_3$ targets, with some cross sections reported here for the first time. The half-lives of La radioisotopes were also determined and compared with the literature values. The resulting data were used to optimize the production parameters for ^{133}La and ^{135}La, and several irradiation tests were carried out to validate our findings.

1. Introduction

The theranostic approach in nuclear medicine relies on pairs of radionuclides, one for diagnosis and one for therapy, targeting the same molecular vector. This strategy enables simultaneous treatment and imaging of disease, providing information on uptake, distribution, and therapeutic response. For maximum effectiveness, theranostic pairs must exhibit nearly identical chemical behavior, ideally belonging to the same element. In this context, lanthanum has attracted increasing interest due to the availability of β^+-emitting radionuclides for Positron Emission Tomography (PET) imaging (^{132}La, $t_{1/2}$ = 4.59 h (Abel et al., 2018), and ^{133}La, $t_{1/2}$ = 3.91 h (Khazov et al., 2011)) and a therapeutic radionuclide (^{135}La, $t_{1/2}$ = 18.91 h (Abel et al., 2018)). The former two are particularly attractive as diagnostic partners for ^{225}Ac, due to their similar ionic radii and resulting comparable coordination chemistry, which facilitates the development of radiopharmaceuticals with analogous targeting properties (Nelson et al., 2022).

^{133}La has a lower mean positron energy compared to ^{132}La (0.46 MeV vs. 1.29 MeV) and other radiometals used for PET imaging such as ^{68}Ga and ^{44}Sc, resulting in a shorter positron range in tissue and consequently improved spatial resolution. In addition, the absence of high-energy gamma emissions reduces the radiation dose to healthy tissues and minimizes potential degradation of image quality. However, the positron emission branching ratio of ^{133}La is relatively low (7.2% (IAEA)), which may require a slightly higher injected activity to achieve sufficient PET signal (Nelson et al., 2023). Importantly, modern long axial-field-of-view (LAFOV) PET scanners provide substantially increase sensitivity, enabling high-quality imaging even for radionuclides with low β^+ branching ratios (Dimitrakopoulou-Strauss et al., 2023).

^{135}La decays by electron capture (EC) to the ground state of ^{135}Ba, emitting Auger electrons with high linear energy transfer (LET) of 4–26 keV/μm (Pedersen et al., 2023). These electrons deposit their

* Corresponding author at: Albert Einstein Center for Fundamental Physics (AEC), Laboratory for High Energy Physics (LHEP), University of Bern, Sidlerstrasse 5, CH-3012 Bern, Switzerland.
E-mail address: gaia.dellepiane@unibe.ch (G. Dellepiane).

https://doi.org/10.1016/j.apradiso.2026.112727
Received 3 March 2026; Received in revised form 26 May 2026; Accepted 26 May 2026
Available online 1 June 2026

Table 1
Decay properties of lanthanum radioisotopes (IAEA). The values in parentheses are the uncertainties referred to the last digits of the value.

Radioisotope	$t_{1/2}$	Decay mode: [%]	E_γ [keV]	BR [%]
^{131}La	59*(2)* min	EC + β^+: 100	108.081*(5)*	25.0*(8)*
^{132g}La	4.59*(4)* h (Abel et al., 2018)	EC + β^+: 100	464.55*(3)*	76*(6)*
^{132m}La	24.3*(5)* min	IT: 76	135.8*(2)*	49*(4)*
		EC + β^+: 24	464.55*(3)*	21.6*(14)*
^{133}La	3.912*(8)* h	EC + β^+: 100	302.38*(4)*	1.61*(8)*
^{134}La	6.45*(16)* min	EC + β^+: 100	604.721*(2)*	5.04*(20)*
^{135}La	18.91*(2)* h (Abel et al., 2018)	EC + β^+: 100	480.51*(2)*	1.52*(24)*
^{136}La	9.87*(3)* min	EC + β^+: 100	818.51*(4)*	2.3*(1)*

kinetic energy over subcellular distances, producing dense ionization tracks that can induce severe DNA damage. When delivered to tumor cells through appropriate targeting vectors, this highly localized energy deposition results in effective cancer cell killing while limiting damage to surrounding healthy tissue. Auger electron emitters are therefore particularly promising for the treatment of diffuse or disseminated disease, where other nuclear emissions, such as β^- particles, do not deliver adequate dose to the targeted cells due to excessive particle range (Buchegger et al., 2006). The 480.5 keV γ-ray (1.5%) accompanying the Auger cascade could also be used for Single Photon Emission Computed Tomography (SPECT) imaging (Fonslet et al., 2017).

^{133}La and ^{135}La can be produced via proton irradiation of enriched ^{134}Ba and ^{135}Ba targets, respectively, using medium-sized medical cyclotrons (up to 25 MeV maximum energy). The irradiation energy must be carefully optimized to maximize the production yield while minimizing the formation of other lanthanum isotopes; defining these optimal irradiation conditions represents one of the main objectives of this work.

In the strategic framework of the Tera-Care Foundation, which aims to advance cancer care trough the development of high-impact accelerator-based medical technologies in collaboration with CERN and other institutions, a dedicated research program is being carried out to identify and characterize novel radionuclides of interest for theranostic applications in nuclear medicine. In this context, and as a part of the preparatory studies for the Clinical Helium Facility for Switzerland (CHeFS) project, the production of ^{133}La and ^{135}La was investigated at the Bern Medical Cyclotron laboratory by irradiating enriched $^{134}BaCO_3$ and enriched $^{135}BaCO_3$ targets, respectively.

Proton irradiation of barium targets produces several lanthanum radioisotopes, which must be taken into account when optimizing the production of the desired radionuclide. The main physical characteristics of these isotopes are summarized in Table 1.

In this paper, we report on the cross-section measurements performed by irradiating natural $BaCO_3$, enriched $^{134}BaCO_3$, and enriched $^{135}BaCO_3$ targets. The contribution to the cross section of each nuclear reaction leading to the production of lanthanum radioisotopes in the energy range up to 18 MeV was determined using a method based on the inversion of a linear system of equations and some of the measured cross section are reported here for the first time.

Given the discrepancies between literature sources, such as the Nuclear Data Sheets (NDS) (Khazov et al., 2005, 2011; Sonzogni, 2004; Singh et al., 2008; Mccutchan, 2018) and Abel et al. (2018), for the half-lives of key lanthanum radionuclides, particularly ^{132}La and ^{135}La, we also measured the half-lives of the main lanthanum isotopes to ensure reliable activity calculations and to select appropriate values for subsequent analyses.

Based on these results, production yields and radionuclide purities for ^{133}La and ^{135}La were evaluated to determine optimal irradiation parameters. Several irradiation tests were then performed to validate and confirm the proposed production strategies.

2. Materials and methods

The Bern Medical Cyclotron laboratory, located at the Bern University Hospital (Inselspital) (Braccini, 2013), hosts an IBA Cyclone 18/18 high current cyclotron capable of producing 18 MeV proton beams with currents ranging from a few pA up to 150 μA (Auger et al., 2015) through eight exit ports. The key feature of the facility is a second bunker with independent access, which allows multidisciplinary research activities to be performed in parallel with the routine production of radiopharmaceuticals. The beam is delivered to the second bunker via a 6-m-long external Beam Transfer Line (BTL), which was used for the measurements presented in this work. The BTL is equipped with beam focusing, steering and diagnostic systems to adjust and monitor the beam position and shape, including a nondestructive two-dimensional beam profiler, named UniBEaM, developed by LHEP and commercialized by D-Pace (Auger et al., 2016; Potkins et al., 2017). This detector is based on scintillating doped silica fibers passing through the beam.

The produced activities were measured with a N-type high purity germanium (HPGe) detector (Canberra2019), coupled to a preamplifier and to a Lynx digital signal analyzer. The energy spectrum of the source was acquired using Genie2k (Mirion Technologies, 2022) for single measurements, and with the Excel2Genie (Forgács et al., 2014) Microsoft Excel application for repeated measurements over time. Spectral analysis was performed with the InterSpec (Sandia National Laboratories) software, developed by Sandia National Laboratories. The HPGe efficiency calibration followed international standards (International Standard, 2021), using a multi-peak γ source containing ^{57}Co, ^{60}Co, ^{85}Sr, ^{88}Y, ^{109}Cd, ^{133}Sn, ^{137}Cs, and ^{241}Am. The calibration source had the same size and geometry as the targets and was measured at distances up to 10 cm from the detector using a custom-designed plexiglass ladder with 1 cm spacing between levels. At each level, the measured efficiencies as a function of γ-ray energy were fitted using a parametric least-squares method. The resulting efficiency curve yields a full-energy peak efficiency of 0.01308(31) at 1 MeV for a source-to-detector distance of 2 cm. Metrological studies (Durán et al., 2022) confirmed that the efficiency uncertainties were below 3% (Juget et al., 2023).

To investigate the cross sections of reactions producing La radioisotopes in the energy range of interest, natural $BaCO_3$ (supplied by Carl Roth), enriched $^{134}BaCO_3$ and enriched $^{135}BaCO_3$ (purchased from Trace Science International) were used. For the production tests, only the enriched materials were irradiated. The enriched samples were characterized by an independent measurement using Inductively Coupled Plasma Mass Spectrometry (ICP-MS) at the Chemistry and Biochemistry Department (DCB) of the University of Bern. The resulting isotopic compositions are reported in Table 2. The abundances of natural $BaCO_3$ follow the values recommended by the Commission on Isotopic Abundances and Atomic Weights (CIAAW).

2.1. Materials and procedures for cross-section measurements

The three $BaCO_3$ materials used in this work were available in powder form. Targets for cross-section measurements were prepared

Table 2
Isotopic abundances of natural $BaCO_3$, enriched $^{134}BaCO_3$ and $^{135}BaCO_3$ used in this work. The natural abundances are derived from the CIAAW, while the enriched materials were characterized via ICP-MS at the University of Bern.

	^{130}Ba	^{132}Ba	^{134}Ba	^{135}Ba	^{136}Ba	^{137}Ba	^{138}Ba
nat.$BaCO_3$ [%]	0.11*(1)*	0.10*(1)*	2.42*(15)*	6.59*(10)*	7.85*(24)*	11.23*(23)*	71.70*(29)*
enr.$^{134}BaCO_3$ [%]	0.005*(1)*	0.009*(1)*	84.242*(41)*	6.116*(15)*	1.578*(4)*	1.440*(4)*	6.610*(35)*
enr.$^{135}BaCO_3$ [%]	0.0011*(1)*	0.0037*(3)*	0.190*(2)*	93.338*(49)*	3.135*(9)*	0.742*(10)*	2.590*(28)*

using the sedimentation method on aluminum discs (22.8 mm in diameter, 2 mm thick), as in our previous publications (Dellepiane et al., 2022). A few milligrams of $BaCO_3$ were suspended in absolute ethanol (EtOH) and deposited in the 4.2-mm-diameter, 0.8-mm-deep pocket in the middle of the disc. Once the ethanol had completely evaporated, the remaining $BaCO_3$ mass was assessed by means of an analytical scale (Shimadzu AUW120D), with a readability of 0.01 mg and a repeatability of 0.02 mg. The pocket was then sealed with a 13-μm thick aluminum foil, taped on the disc to prevent the material escape before and during the irradiation. With this procedure, target thicknesses of a few tens of μm were achieved, allowing the energy to be considered constant within the uncertainty over the full irradiated mass.

Each target was then irradiated with the same experimental procedure used in our previous studies on cross-section measurements (Dellepiane et al., 2021). This method is based on the irradiation of the full mass of a thin target by a proton beam with a flat beam profile and has the advantage that the target has not to be necessarily uniform in thickness, provided that the energy of the protons can be considered constant within its mass.

The beam was flattened by the optical elements of the BTL and monitored with the UniBEaM detector. The beam current hitting the target material was measured by means of a custom target station connected to an electrometer (B2985A Keysight). The station provides a beam of controlled diameter thanks to a 6-mm diameter collimator and it is equipped with an electron suppressor ring connected to a negative bias voltage to repel secondary electrons produced during the irradiation.

To perform irradiations below 18 MeV, the beam energy was degraded by means of aluminum attenuator discs with thicknesses of 125, 200, and 300 μm placed in front of the target. These discs were combined to obtain several effective thicknesses ranging from 200 μm to 1650 μm. The resulting proton energy was determined using the SRIM-2013 Monte Carlo code (Ziegler and Manoyan, 2013).

After each irradiation, the target was measured with the HPGe detector, and the cross sections of La radioisotopes as a function of the proton energy were determined using the equation:

$$\sigma(E) = A(t_{EOB}) \cdot \frac{q}{dI/dS} \cdot \frac{1}{m} \cdot \frac{m_{mol}}{N_A \epsilon \eta} \cdot f_C \tag{1}$$

where $A(t_{EOB})$ is the activity at the End of Beam (EOB), q is the elementary charge, dI/dS is the current on target per unit surface, m is the target material mass, m_{mol} is the molar mass of the material, N_A is the Avogadro number, ϵ is the isotopic ratio of the target nucleus and η its stoichiometric number.

The correction factor

$$f_C = \frac{\int_{t_{SOB}}^{t_{EOB}} I(t')dt'}{e^{-\lambda(t_{EOB}-t_{SOB})} \int_{t_{SOB}}^{t_{EOB}} e^{\lambda t'} I(t')dt'} \tag{2}$$

accounts for the decay of the radionuclides (with decay constant λ) during the irradiation, where $I(t')$ is the current on target at time t' and t_{SOB} is the time at the Start of Beam (SOB).

In the case where the current on target can be considered constant, the correction factor simplifies to

$$f_C = \frac{\lambda t_i}{1 - e^{-\lambda t_i}} \tag{3}$$

where $t_i = t_{EOB} - t_{SOB}$ is the irradiation time.

The more general form of f_C is necessary for short-lived radionuclides, i.e. ^{134}La and ^{136}La, for which variations in beam current at different times during irradiation have significant effects on the activity produced.

For La radioisotopes whose production is the result of two nuclear processes, it was necessary to decouple their contributions to the production cross section. For this purpose, a method based on the inversion of a linear system of equations was used. This method is described in our previous publications (Braccini et al., 2022) and requires measuring the total cross section with as many materials, with different isotopic compositions, as the number of reactions involved in the production of the radionuclide under investigation. Considering two materials A and B with different known isotopic compositions, in the case of two reactions (p,x) and (p,y) starting from the ith and jth isotope, respectively, the following linear system holds for a given beam energy :

$$\begin{cases} \sigma^A_{TOT} = \beta^A_i \cdot \sigma(p,x) + \beta^A_j \cdot \sigma(p,y) \\ \sigma^B_{TOT} = \beta^B_i \cdot \sigma(p,x) + \beta^B_j \cdot \sigma(p,y) \end{cases} \tag{4}$$

where the experimentally measured production cross sections appear on the left side of the equations and the reaction cross sections to be determined on the right. $\beta^{A,B}_{i,j}$ is the abundance of the target isotope in the considered material.

2.2. Study of ^{133}La and ^{135}La production yield and radionuclidic purity

With the aim of optimizing the production of ^{133}La and ^{135}La from enriched $^{134}BaCO_3$ and $^{135}BaCO_3$ targets, respectively, a study of the Thick Target Yield (TTY) and the resulting radionuclidic purity was performed. Based on the measured cross sections, the expected TTY as a function of the proton energy on target E is defined as the producible activity per unit current and time (GBq/μAh) and can be calculated as

$$TTY(E) = f_C \cdot \frac{N_A \epsilon \eta}{m_{mol} \cdot q} \int_{E_{th}}^{E} \frac{\sigma(E')}{S_p(E')} dE' \tag{5}$$

where f_C is the correction factor defined in Eq. (2), $\sigma(E')$ the cross section as a function of the proton kinetic energy E', $S_p(E')$ is the mass stopping power for the target material and E_{th} is the threshold energy of the considered reaction. The mass stopping power is calculated using the SRIM code.

For thin targets, in which protons are not fully stopped, the production yield $Y(E)$ can be expressed as

$$Y(E) = TTY(E) - TTY(E_{out}) \tag{6}$$

where E_{out} is the proton energy after the target, as determined by SRIM simulations.

For a sample containing a mixture of N radioisotopes, the radionuclidic purity P of the radionuclide of interest X is defined as

$$P_X = \frac{A_X}{\sum_i^N A_i} \tag{7}$$

where A_i is the activity of the ith radionuclide.

2.3. Materials and procedures for ^{133}La and ^{135}La production tests

Targets for the production of ^{133}La and ^{135}La were prepared by compressing approximately 45 mg of enriched $^{134}BaCO_3$ and enriched $^{135}BaCO_3$ powders, respectively, under an axial force of about $4 \cdot 10^4$ N. The density of the pressed material was determined from the measured mass and thickness of each pellet and resulted in (3.2 ± 0.4) g cm^{-3}

and (3.4 ± 0.5) g cm^{-3} for enriched $^{134}BaCO_3$ and enriched $^{135}BaCO_3$, respectively. These values were used in all calculations and SRIM simulations.

The obtained disc-shaped pellets (6 mm in diameter, 0.3 mm thick) were placed inside a dedicated capsule, referred to as *coin*, consisting of two aluminum halves held together by small permanent magnets, described in our previous publications (Dellepiane et al., 2021).

For each enriched material, two production tests were performed using an adapted target holder positioned in the same station employed for cross-section measurements. In this configuration, high beam intensities cannot be achieved due to the absence of a cooling system. The resulting low activity allowed the pellets to be measured immediately after the EOB using the HPGe detector, enabling the detection of the short-lived ^{134}La and ^{136}La without incurring significant dead times. For both enriched materials, the two irradiations were separated by approximately one month to ensure complete decay of all radionuclides produced during the first test.

2.4. Procedure for half-life measurements

The same targets used for the production tests were also employed for the determination of the half-lives of La radionuclides. After each irradiation, the pellets were repeatedly measured with the HPGe detector over extended periods.

For the enriched $^{134}BaCO_3$ material, two measurement schemes were adopted. In the first case, the target was measured every 20 min for approximately 20 h after EOB. In the second case, the pellet was measured every minute for about 50 min after EOB in order to detect the short-lived radionuclides (^{134}La and ^{136}La), and then every 30 min for approximately 24 h.

For the enriched $^{135}BaCO_3$ material, following the first irradiation, the target was measured with variable acquisition times between 0.6 and 2.4 min during the first 20 min after EOB, and then every hour for approximately 150 h. In the second measurement campaign, spectra were acquired every minute during the first 30 min after EOB, followed by measurements every 1.5 h for about 187 h.

The activity of each radionuclide was determined as a function of time, and the corresponding half-life was extracted by fitting the data with a simple exponential decay law

$$A(t) = A(t_{EOB})e^{-\lambda t} \tag{8}$$

with the precision determined entirely by statistics.

The obtained half-life values were compared with experimental data available in the literature. For the subsequent analyses presented in this work, the half-life value associated with the smallest uncertainty was adopted.

3. Data analysis and results

3.1. Half-life measurements

To validate the method used for half-life determination, the half-life of ^{133}La was measured, as it has a well-established and precisely known reference value (Khazov et al., 2011).

Following irradiations of enriched $^{134}BaCO_3$ targets, the activity of ^{133}La was determined by analyzing the 302 keV γ-ray emission. In the second test, measurements with one-minute acquisition times were excluded from the fit due to large statistical fluctuations associated with the short counting intervals.

The measured activities as a function of time, together with the exponential decay fits and corresponding residuals, are shown in Fig. 1.

The final half-life was obtained as the weighted mean of the values from the two independent fits. The results are reported in Table 3 and Fig. 2, together with literature values for comparison. A good

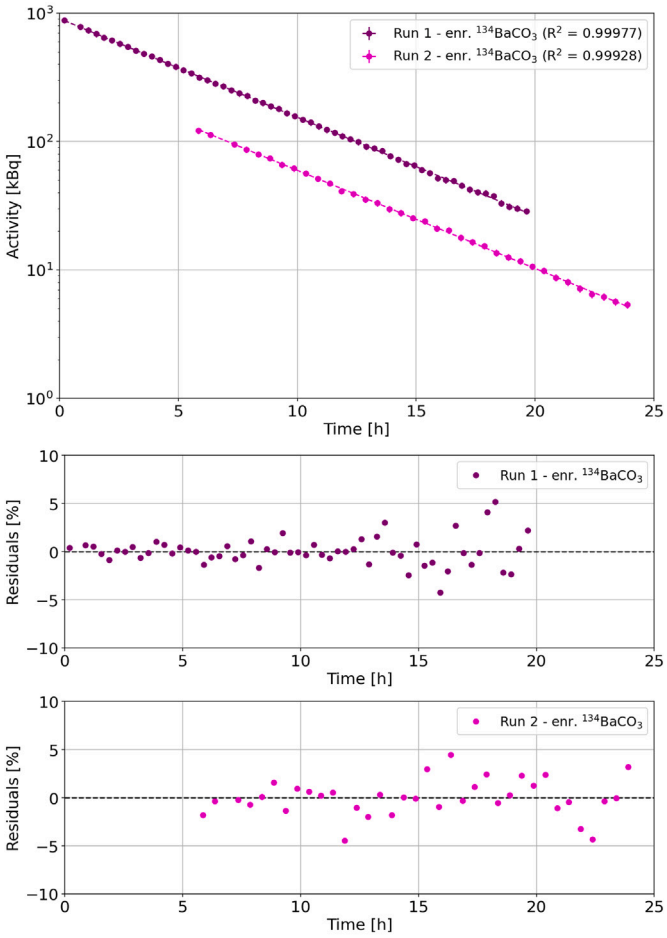

Fig. 1. Activities of ^{133}La measured over time and fit curves with the corresponding residuals.

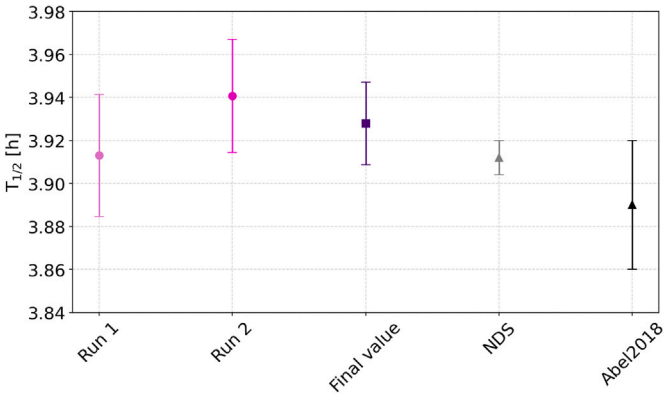

Fig. 2. Half-life values for ^{133}La.

agreement within the uncertainties is observed with both the recommended NDS value (Khazov et al., 2011) and with the experimental value reported by Abel et al. (2018)

The half-life of ^{132}La was determined from the enriched $^{135}BaCO_3$ target by analyzing the 464.6 keV γ-ray emission. This line is also present in the EC/β^+ decay of the metastable state ^{132m}La (Table 1), but no evidence of its production was observed and its contribution was considered negligible. Measured activities, exponential decay fits, and residuals are shown in Fig. 3. The final half-life was calculated as the weighted mean of the two independent fits and is reported

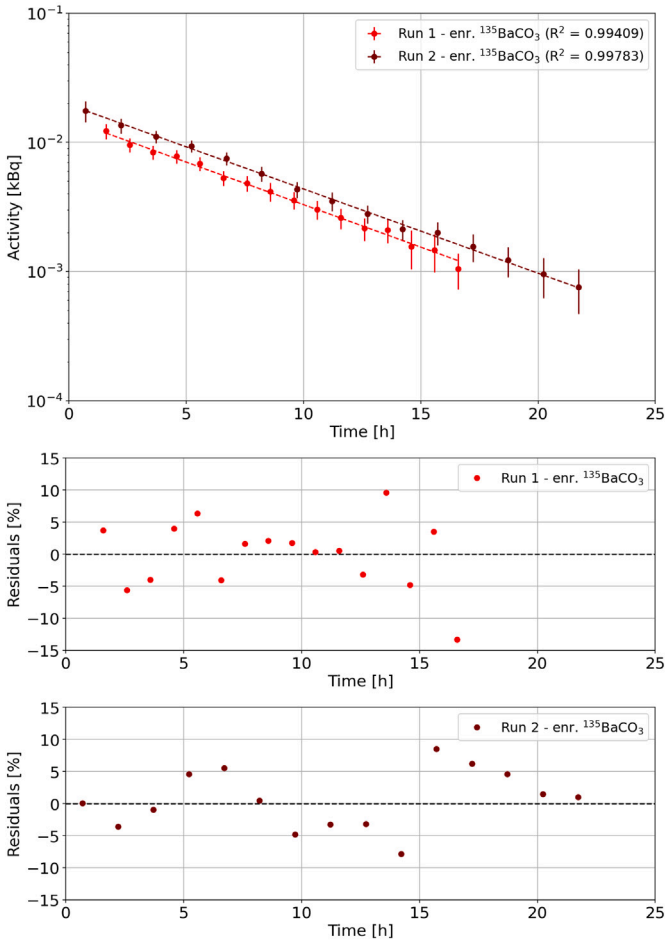

Fig. 3. Activities of ^{132}La measured over time and fit curves with the corresponding residuals.

in Table 4 and Fig. 4, showing good agreement with both the NDS value (Khazov et al., 2005) and the experimental result from Abel et al. (2018). The half-life of ^{134}La was measured in all four irradiations (two tests each with enriched $^{134}BaCO_3$ and $^{135}BaCO_3$) by analyzing the 605 keV γ-ray emission. Activities, fits, and residuals are shown in Fig. 5, and the resulting half-life values are reported in Fig. 6 and Table 5, showing full compatibility with each other and smaller uncertainty than the NDS recommended value (Sonzogni, 2004). The half-life of ^{135}La was determined using the enriched $^{135}BaCO_3$ targets by analyzing the 481 keV γ-ray emission. The measured activities as a function of time, together with the exponential decay fits and the corresponding residuals, are shown in Fig. 7.

The final half-life value, obtained as the weighted mean of the two independent fits, is reported in Table 6 and Fig. 8. The result is compatible within the uncertainties with the experimental value reported by Abel et al. (2018), while it shows a significant discrepancy with the value recommended in the NDS (Singh et al., 2008). Finally, the half-life of ^{136}La was measured only for the enriched $^{135}BaCO_3$ targets. In the case of enriched $^{134}BaCO_3$, it was not possible to acquire a sufficient number of data points to perform a reliable fit. This limitation is attributed to the low intensity of the 818 keV γ-ray line used for the analysis.

The measured activity as a function of time, together with the exponential decay fit and the corresponding residuals, is shown in Fig. 9. The resulting half-life values are reported in Table 7 and Fig. 10, where it is compared with literature data. The value obtained in this work shows full agreement within the uncertainties with the recommended NDS value (Mccutchan, 2018).

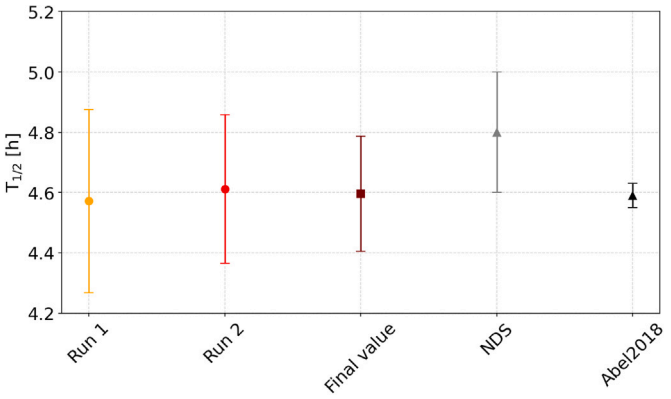

Fig. 4. Half-life values for ^{132}La.

Table 3
Individual and final ^{133}La half-life values. All values are in hours.

Run 1	Run 2	Final value	NDS	Abel 2018
3.91(3)	3.94(3)	3.93(2)	3.912(8)	3.89(3)

Table 4
Individual and final ^{132}La half-life values. All values are in hours.

Run 1	Run 2	Final value	NDS	Abel 2018
4.57(30)	4.61(25)	4.60(19)	4.8(2)	4.59(4)

Table 5
Individual and final ^{134}La half-life values. All values are in minutes.

Run 1	Run 2	Run 3	Run 4	Final value	NDS
6.53(14)	6.50(11)	6.48(17)	6.48(9)	6.49(6)	6.45(16)

Table 6
Individual and final ^{135}La half-life values. All values are in hours.

Run 1	Run 2	Final value	NDS	Abel 2018
19.02(16)	19.07(14)	19.04(10)	19.5(2)	18.91(2)

Table 7
Individual and final ^{136}La half-life values. All values are in minutes.

Run 1	Run 2	Final value	NDS
9.84(70)	9.83(49)	9.84(40)	9.87(3)

3.2. Cross-section measurements

All $BaCO_3$ materials were irradiated for an average time of 11 min with a mean current of about 9 nA. After the EOB, the produced activities were assessed with the HPGe detector. In all measurements, the count frequency was sufficiently low to limit pile-up effects (average dead time below 4%). A representative gamma-ray spectrum acquired for an enriched $^{135}BaCO_3$ target is shown in Fig. 11.

The main experimental uncertainty in the cross-section measurements depended on the specific radionuclide considered. For ^{131}La and ^{132}La, the dominant contribution arose from the statistical uncertainty of the γ-ray peak fitting (~17%), due to the relatively low activity produced. In the case of ^{132m}La, the statistical component was even larger (up to 30%), clearly representing the leading source of uncertainty. To reduce the impact of low-statistics measurements, the same targets were measured more than once, and the final cross-section values were obtained as weighted averages of the independent determinations.

For ^{134}La and ^{135}La, the main contribution originated from the uncertainty in the branching ratio of the selected γ-line (4.0% and 15.8%, respectively), while for ^{133}La and ^{136}La, the dominant contribution was

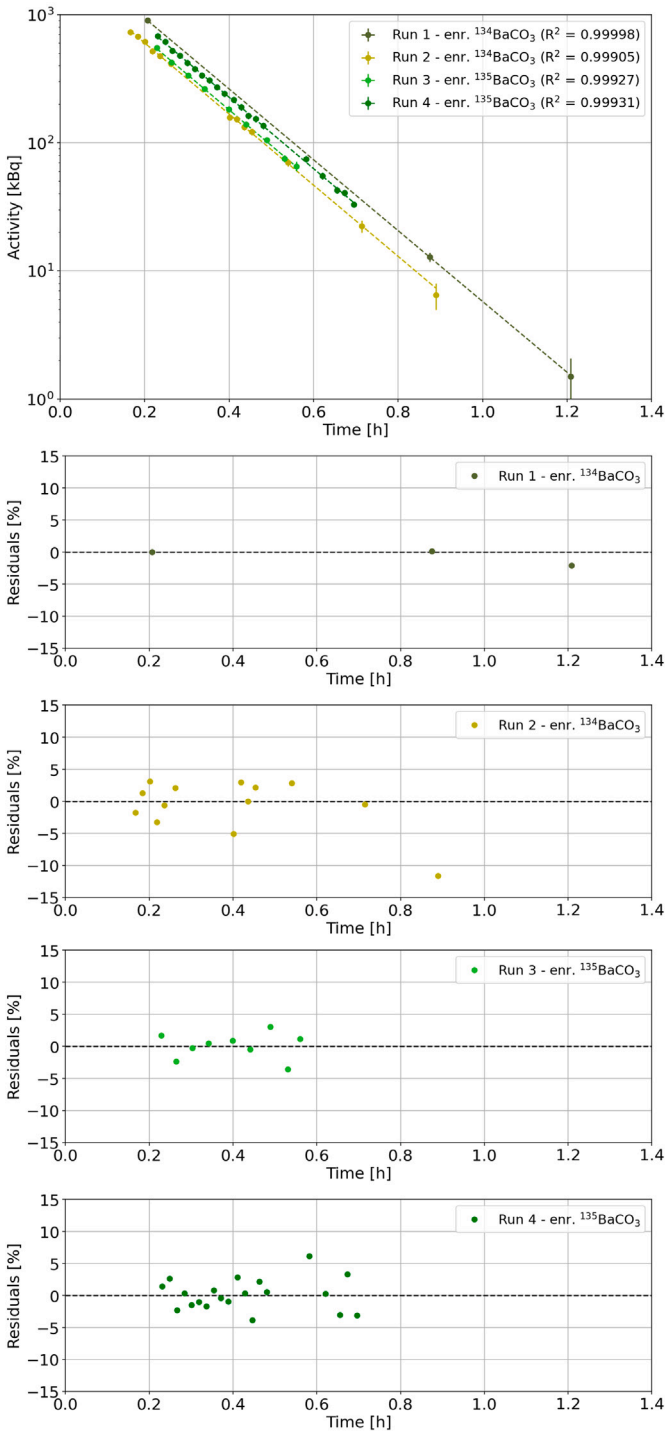

Fig. 5. Activities of ^{134}La measured over time and fit curves with the corresponding residuals.

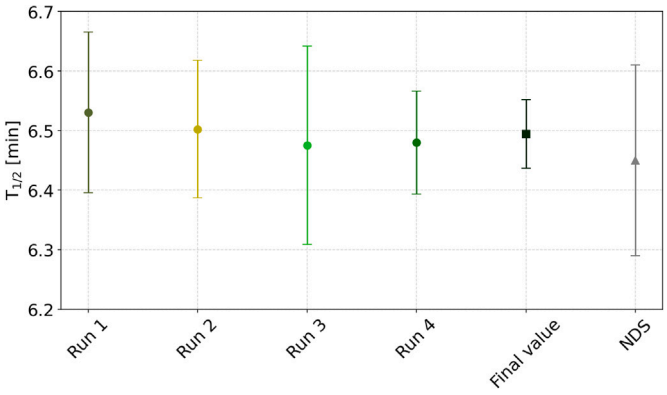

Fig. 6. Half-life values for ^{134}La.

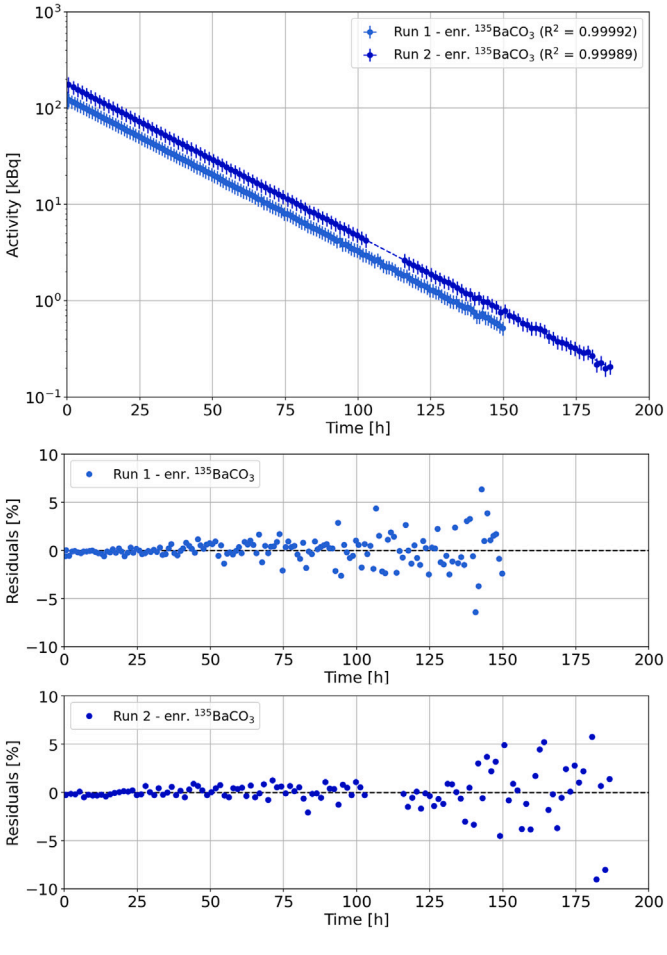

Fig. 7. Activities of ^{135}La measured over time and fit curves with the corresponding residuals.

again associated with the statistical uncertainty of the γ-ray peak fitting (8.7% and 14.8%, respectively).

Additional systematic sources of uncertainty affecting all measurements include the flatness of the beam (5%), the beam current integration (1%), the HPGe detector efficiency (2.5–3.6%, depending on γ-ray energy), and the target mass determination (below 2.7%). The uncertainty associated with the half-life was 3.38% for ^{131}La and 2.05% for ^{132m}La, while it remained below 1% for the other radionuclides. All individual contributions were considered independent and were summed in quadrature to obtain the total experimental uncertainty for each measured cross section.

The uncertainties of the nuclear cross sections obtained by solving the linear system of equations were derived by considering the maximum and minimum values of the production cross sections.

Numerical values of the measured cross sections are provided in the Appendix (Tables 10–18).

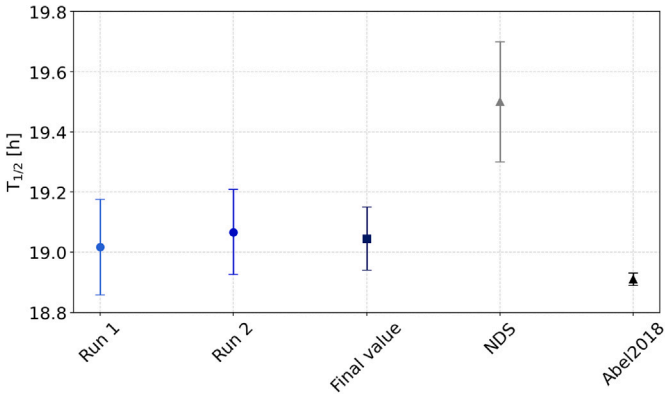

Fig. 8. Half-life values for ^{135}La.

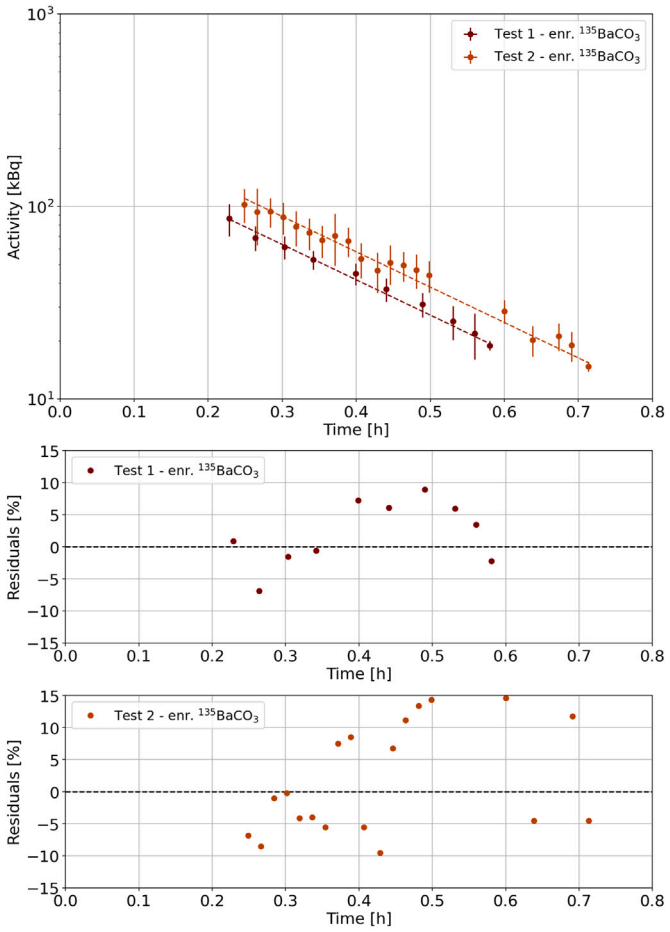

Fig. 9. Activities of ^{136}La measured over time and fit curves with the corresponding residuals.

Lanthanum-131. In the energy range of interest, ^{131}La can be produced via two reactions: ^{130}Ba(p, γ)^{131}La and ^{132}Ba(p,2n)^{131}La. The (p, γ) channel has a very low cross section and ^{130}Ba is present in minute amounts in the irradiated materials; therefore, only the (p,2n) reaction on ^{132}Ba was measured, using natural Ba as target. During irradiation, both the ground state (^{131g}La) and a short-lived metastable state (^{131m}La) are populated. The metastable state decays entirely via IT (100%) to the ground state with a half-life of 170 μs (IAEA). Due to this very short half-life, the reported ^{131g}La cross sections are cumulative.

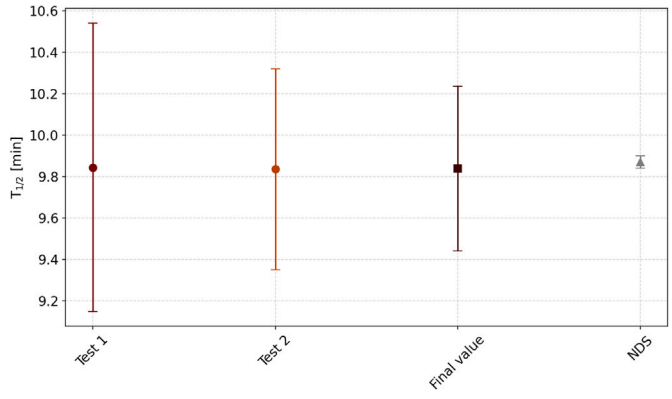

Fig. 10. Half-life values for ^{136}La.

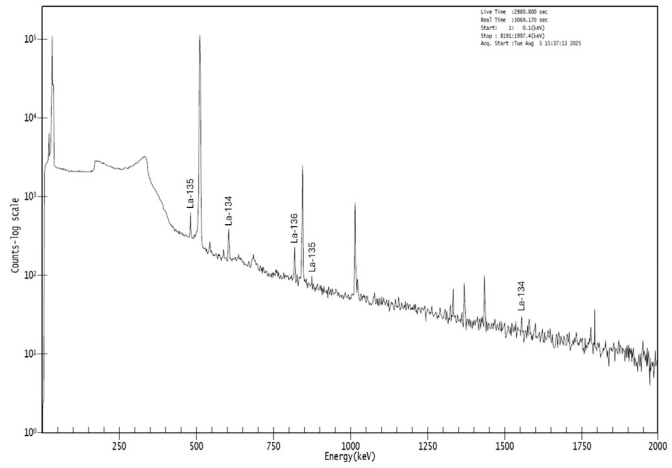

Fig. 11. Representative HPGe gamma-ray spectrum acquired for an enriched $^{135}BaCO_3$ target. The most prominent photopeaks used for radionuclide identification and activity quantification are indicated.

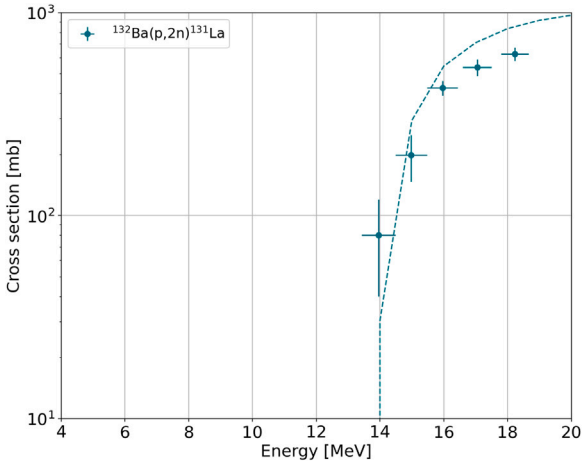

Fig. 12. ^{132}Ba(p,2n)^{131}La nuclear cross sections. The dots are the experimental data, the dashed lines are the TENDL-2025 calculations.

The measured cross sections are shown in Fig. 12 together with TENDL-2025 predictions (Koning and Rochman, 2012), which follow the experimental trend but tend to overestimate the data at high energies. No experimental data from the literature are available.

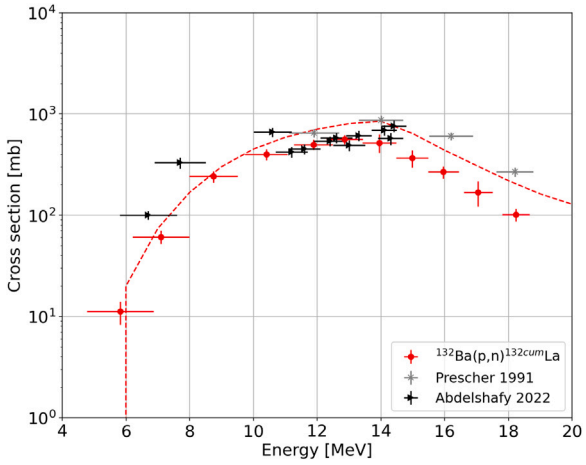

Fig. 13. ^{132}Ba(p,n) ^{132cum}La nuclear cross sections. The dots are the experimental data, the dashed lines are the TENDL-2025 calculations.

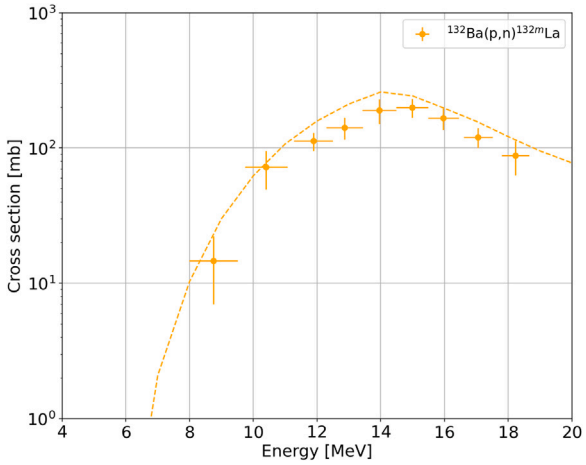

Fig. 14. ^{132}Ba(p,n) ^{132m}La nuclear cross sections. The dots are the experimental data, the dashed lines are the TENDL-2025 calculations.

Lanthanum-132. In the energy range of interest, ^{132}La is mainly produced through the ^{132}Ba(p,n)^{132}La reaction. Both the ground state ($t_{1/2}$ = 4.59 h) and a metastable state ($t_{1/2}$ = 24.3 min) are populated. ^{132m}La decays 76% via IT to ^{132g}La and 24% via EC/β^+ to ^{132}Ba. The IT channel emits a distinct 135 keV γ-ray that can be measured immediately after EoB, while the EC/β^+ channel shares the 464.5 keV γ-ray with the ground state (IAEA). ^{132}La was therefore measured after the metastable state had fully decayed and the reported cross sections are thus cumulative. All measurements were performed using natural barium targets, due to the low isotopic abundance of ^{132}Ba in enriched materials.

The ^{132}Ba(p,n) ^{132cum}La nuclear cross sections are reported in Fig. 13, together with TENDL predictions and the literature data (Prescher et al., 1991; Abdelshafy et al., 2022). A good agreement with TENDL is observed at low energies; above 13 MeV the TENDL predictions tend to overestimate the experimental values. Literature data agree only near the peak (10–14 MeV), whereas at lower and higher energies they are higher than our measurements. No literature data exist for the ^{132}Ba(p,n) ^{132m}La cross section (Fig. 14).

Lanthanum-133. Up to 18 MeV, ^{133}La is produced via the ^{134}Ba(p,2n)^{133}La reaction. Cross-section measurements using natural $BaCO_3$ and enriched $^{134}BaCO_3$ targets are shown in Fig. 15, along with TENDL predictions and literature data (Prescher et al., 1991). Results from both target materials are fully consistent withing uncertainties and generally well described by TENDL predictions, which slightly underestimates the measured values. In contrast, the data reported by Prescher et al. show noticeable deviations from our results.

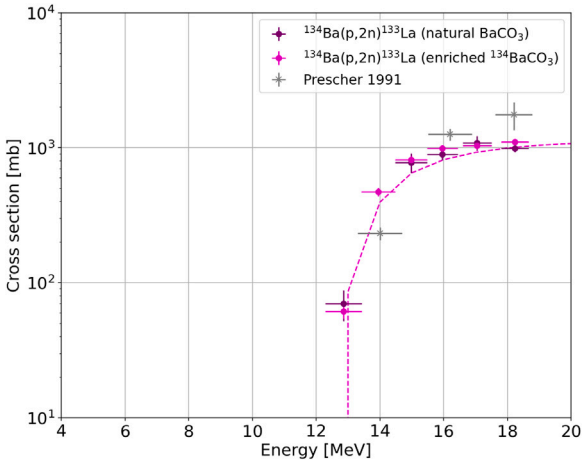

Fig. 15. ^{134}Ba(p,2n)^{133}La nuclear cross sections. The dots are the experimental data, the dashed lines are the TENDL calculations.

Lanthanum-134. Two reactions contribute to ^{134}La production in the energy range of interest, namely ^{134}Ba(p,n)^{134}La and ^{135}Ba(p,2n)^{134}La. During the irradiation, both the ground state and a metastable state of ^{134}La are populated; however, ^{134m}La decays to ^{134g}La via IT (100%) with a half-life of 29 μs (IAEA) and could not be detected. The cross sections reported in this study are therefore cumulative.

Measurements were performed with all three materials (natural BaCO3, enriched ^{134}BaCO3, and enriched $^{135}BaCO_3$) as shown in Fig. 16. The cross sections for individual reactions were extracted using the linear system method (Section 2.1), using the combinations nat & enr^{134} and enr^{134} & enr^{135}. Once it was verified that the results from the two sets of measurements were fully compatible within uncertainties, weighted averages were used as final values. The resulting ^{134}La reaction cross sections are reported in Fig. 17.

Only two sets of data for the (p,n) channel are available in the EXFOR database (Muminov et al., 1980; Vasidov et al., 1981), and both significantly underestimate our results. To the best of our knowledge, no other measurements exist for the (p,2n) channel. TENDL reproduces the (p,n) reaction reasonably well, while overestimating (p,2n) results at higher energies.

Lanthanum-135. In the investigated energy range, ^{135}La is produced via the ^{134}Ba(p, γ), ^{135}Ba(p,n) and ^{136}Ba(p,2n) reactions. However, the cross section of the (p, γ) channel is extremely low and therefore negligible, even when using enriched $^{134}BaCO_3$.

The contributions of (p,n) and (p,2n) reactions were disentangled using the linear system method with natural and enriched $^{135}BaCO_3$ targets (Fig. 18). The resulting reaction cross sections, shown in Fig. 19, agree well with TENDL predictions and with literature data (Khomenko et al., 2024).

Lanthanum-136. In the energy range of interest, three reactions contribute to ^{136}La: ^{135}Ba(p, γ)^{136}La, ^{136}Ba(p,n) ^{136}La, and ^{137}Ba(p,2n)^{136}La. Also in this case, the (p, γ) contribution is negligible, even when considering enriched $^{135}BaCO_3$.

During the irradiation, both the ground state and a metastable state of ^{136}La are populated; however, ^{136m}La decays to ^{136g}La via IT (100%) with a half-life of 114 ms (IAEA). The cross sections reported in this study are therefore cumulative.

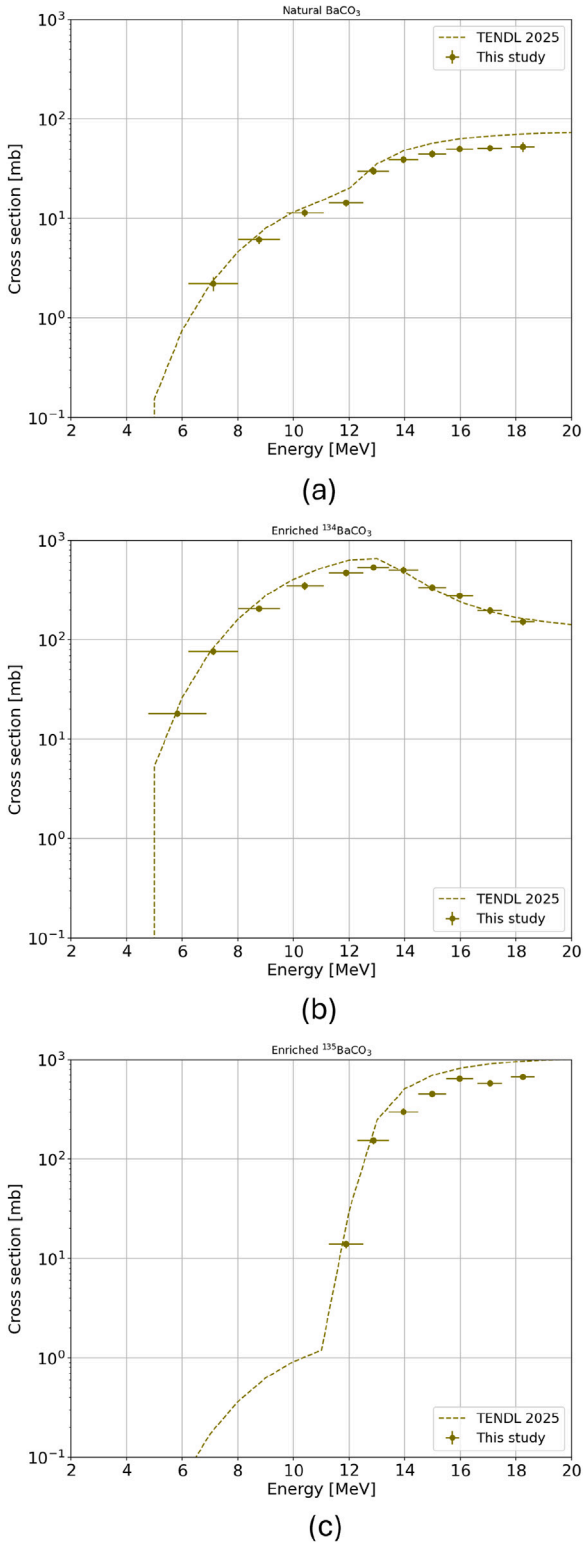

Fig. 16. ^{134}La production cross section from natural $BaCO_3$ (a), enriched $^{134}BaCO_3$ (b) and enriched $^{135}BaCO_3$ (c), whose isotopic composition is reported in Table 2. The dots are the experimental data, the dashed lines are the TENDL-2025 calculations.

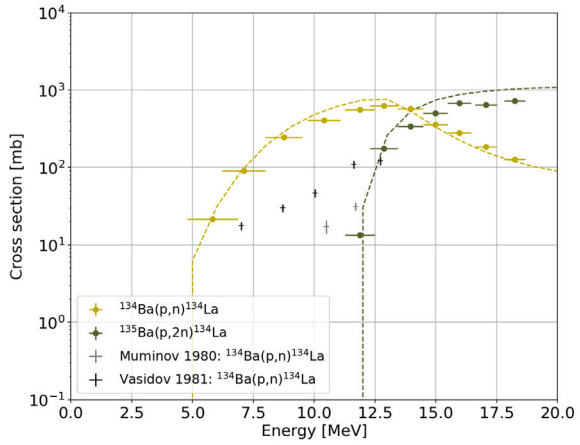

Fig. 17. ^{134}Ba(p,n)^{134}La and ^{135}Ba(p,2n)^{134}La nuclear cross sections. The dots are the experimental data, the dashed lines are the TENDL-2025 calculations.

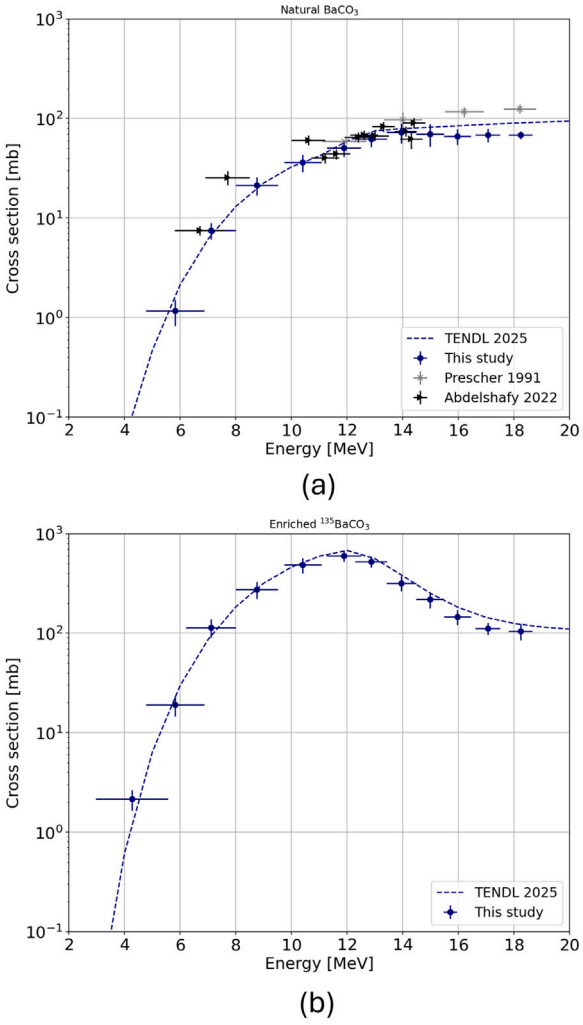

Fig. 18. ^{135}La production cross section from natural $BaCO_3$ (a) and enriched $^{135}BaCO_3$ (b), whose isotopic composition is reported in Table 2. The dots are the experimental data, the dashed lines are the TENDL-2025 calculations.

To disentangle the contributions of (p,n) and (p,2n) channels, the production cross section measured from natural $BaCO_3$ and enriched $^{135}BaCO_3$ targets, shown in Fig. 20, were used. The results are presented in Fig. 21, along with TENDL calculations and literature data (Vasidov et al., 1981). While our data are generally consistent with TENDL, literature values deviate significantly.

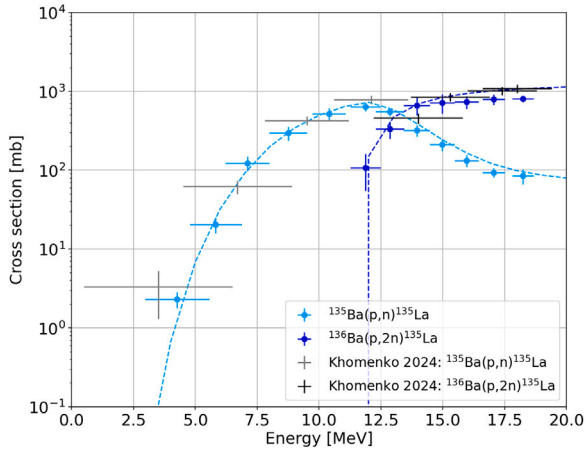

Fig. 19. ^{135}Ba(p,n)^{135}La and ^{136}Ba(p,2n)^{135}La nuclear cross sections. The dots are the experimental data, the dashed lines are the TENDL-2025 calculations.

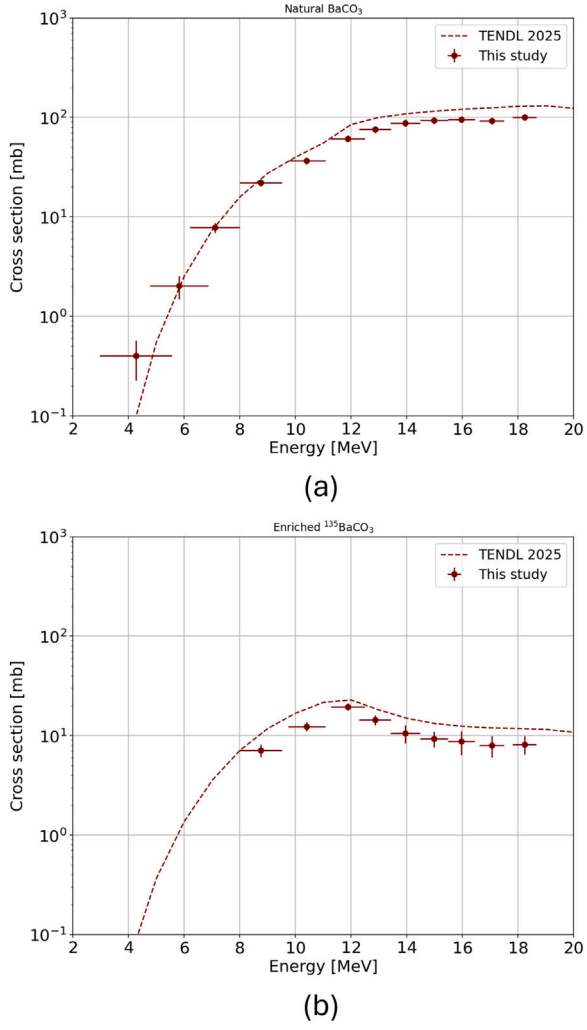

Fig. 20. ^{136}La production cross section from natural $BaCO_3$ (a) and enriched $^{135}BaCO_3$ (b), whose isotopic composition is reported in Table 2. The dots are the experimental data, the dashed lines are the TENDL-2025 calculations.

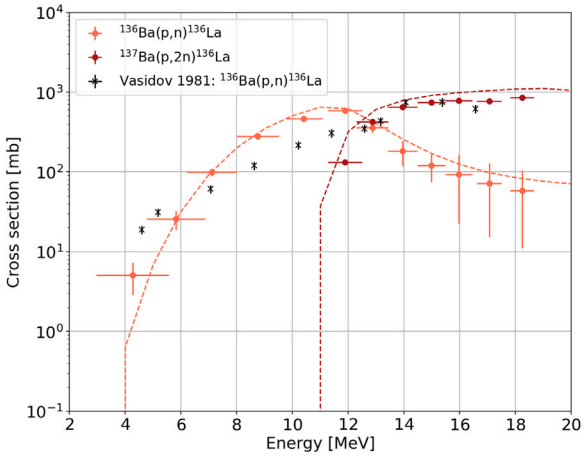

Fig. 21. ^{136}Ba(p,n)^{136}La and ^{137}Ba(p,2n)^{136}La nuclear cross sections. The dots are the experimental data, the dashed lines are the TENDL-2025 calculations.

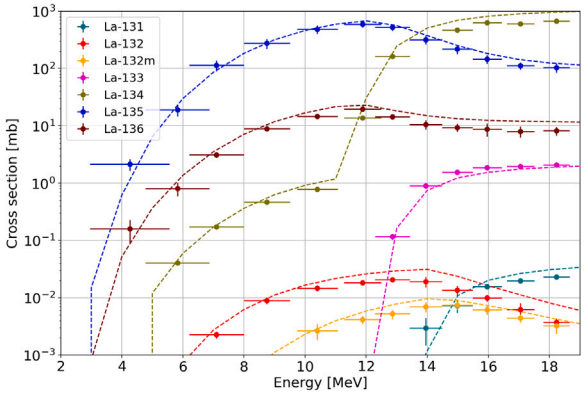

Fig. 22. Production cross sections of La radioisotopes irradiating a 93.3% enriched $^{135}BaCO_3$ target (see Table 2). The dots are the experimental data, the dashed lines are the TENDL-2025 calculations.

3.3. *^{135}La optimized production*

Knowing the cross sections of all nuclear reactions producing lanthanum radioisotopes up to 18 MeV, the corresponding production cross sections were calculated for an enriched $^{135}BaCO_3$ target (isotopic composition reported in Table 2) and are shown in Fig. 22. Based on these data, the TTYs of La radioisotopes were evaluated as a function of the proton entry energy using Eq. (5), assuming an irradiation time of 1 h, as shown in Fig. 23. The main radionuclidic impurities are ^{134}La and ^{136}La; however, both have half-lives shorter than 10 min and can be efficiently removed by allowing a short cooling time after irradiation (on the order of 1–2 h). The only impurity with a non-negligible half-life is ^{133}La; thus, the incident proton energy should be kept below 14 MeV to minimize its production. Under these conditions, the TTY of ^{135}La is 0.08 GBq/μA. The radionuclidic purity, calculated from Eq. (7), reaches 99.9% approximately 2 h after EOB, when the residual activity remains above 90% (Fig. 24). Consequently, the time between production and patient administration is expected to be governed only by the duration of radiochemical processing and transportation.

Owing to the relatively long ^{135}La half-life, the TTY can be significantly increased by extending the irradiation time. Fig. 25 shows the TTY for a 10-h irradiation. At 14 MeV, the TTY of ^{135}La reaches 0.67 GBq/μA, while the increase in ^{133}La production remains negligible. As a result, the radionuclidic purity after 2 h from EOB remains above 99.9% (Fig. 26).

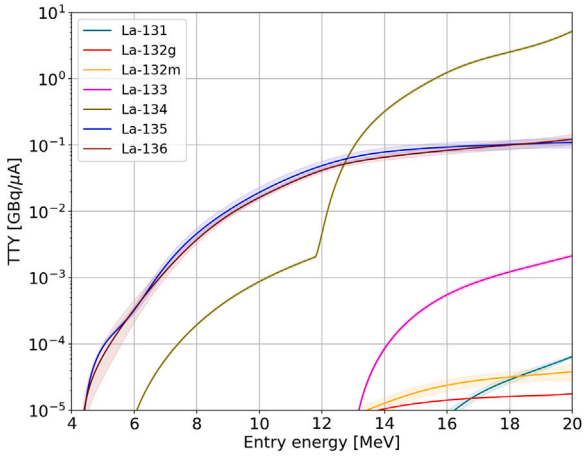

Fig. 23. Thick target yields of La radioisotopes as a function of the proton entry energy, irradiating a 93.3% enriched $^{135}BaCO_3$ target. The irradiation time is set to 1 h.

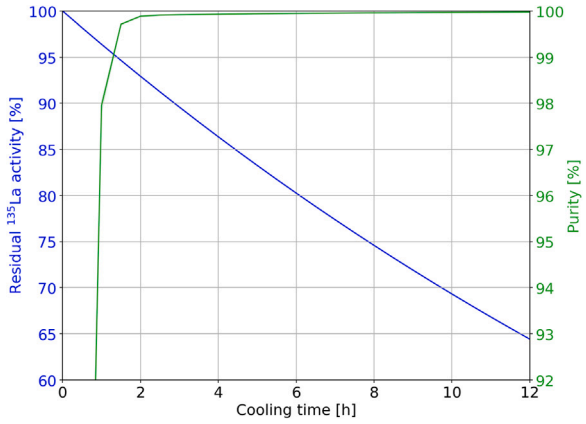

Fig. 24. ^{135}La residual activity and radionuclidic purity as a function of cooling time after 1-h irradiation.

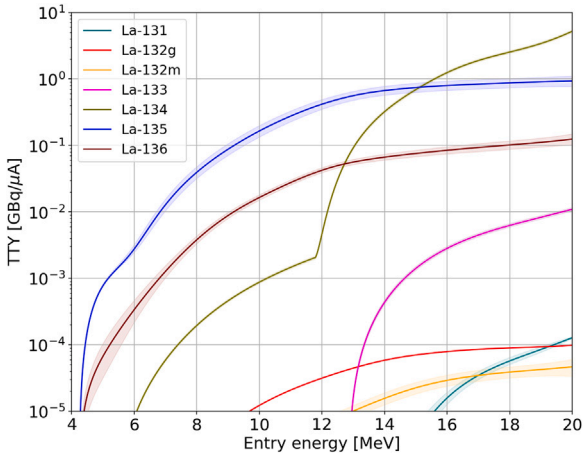

Fig. 25. Thick target yields of La radioisotopes as a function of the proton entry energy, irradiating a 93.3% enriched $^{135}BaCO_3$ target. The irradiation time is set to 10 h.

It is nevertheless important to remark that, in order to achieve a high labeling efficiency, non-radioactive impurities produced during irradiation must also be carefully assessed and, if necessary, minimized,

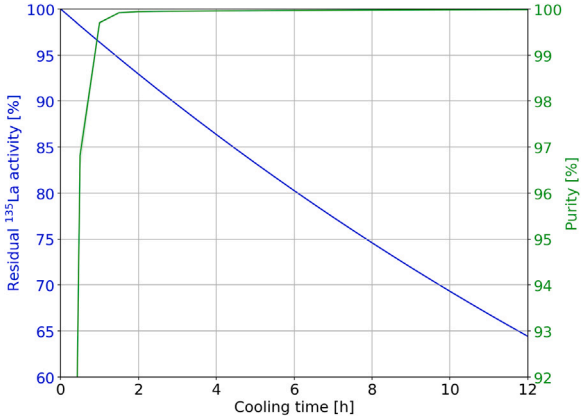

Fig. 26. ^{135}La residual activity and radionuclidic purity as a function of cooling time after 10-h irradiation.

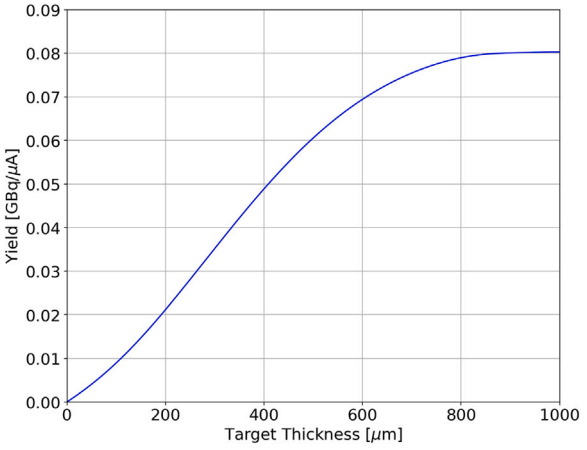

Fig. 27. ^{135}La yield as a function of the target thickness. The irradiation time is set to 1 h.

as they may interfere with ^{135}La during the radiolabeling procedure. Further studies are required to address this aspect.

To define the optimal target thickness, the physical yield was calculated using Eq. (6) as a function of target thickness for a 1-h irradiation (Fig. 27). The yield reaches a maximum of 0.08 GBq/μA for an 850-μm-thick target, corresponding to about 83 mg of material. However, by selecting thicknesses of 450–500 μm, the yield is reduced by only about 27%, while the required amount of target material decreases by approximately 44%, thus significantly reducing costs. Based on these considerations, a 0.46-mm-thick target, corresponding to about 43 mg of material, was selected for experimental tests. The pellet was irradiated twice at an incident energy of (13.6 ± 0.5) MeV, with an interval of approximately one month between irradiations to allow complete decay of all radionuclides produced in the first run.

The incident energy, irradiation parameters, and the activities measured with the HPGe detector are reported in Table 8, along with the expected activities calculated from the measured cross sections. In almost all cases, good agreement within uncertainties is observed. For ^{134}La, the measured activity is nearly twice the expected value. This discrepancy is most likely due to the fact that the investigated energy range lies close to the threshold of the ^{135}Ba(p,2n)^{134}La reaction, where small variations in the incident energy result in large changes in the cross section and, consequently, in the produced activity. Regarding ^{135}La, the two production tests provided yields of (0.062 ± 0.003) GBq/μAh and (0.064 ± 0.003) GBq/μAh, with radionuclidic purities 2 h after EOB of

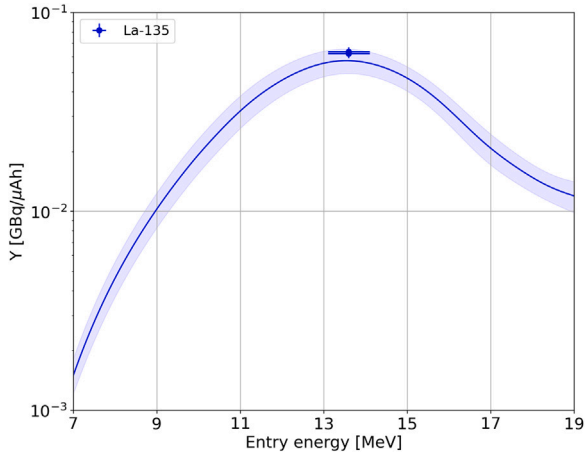

Fig. 28. ^{135}La yields calculated from the measured cross sections in our irradiation conditions compared with the experimental results.

Table 8
Irradiation parameters and La activities at EOB obtained irradiating a 0.46-mm-thick enriched $^{135}BaCO_3$ pellet. Values in parentheses are calculated from measured cross sections.

	Test 1	Test 2
E_{in} [MeV]	13.6 ± 0.5	13.6 ± 0.5
t_i [min]	21.3	22.7
I [nA]	5.7	7.6
Activity [kBq]		
^{131}La	Not Detected *(–)*	Not Detected *(–)*
^{132}La	0.015 ± 0.001 *(0.016 ± 0.004)*	0.020 ± 0.001 *(0.023 ± 0.005)*
^{132m}La	Not Detected *(0.03 ± 0.01)*	Not Detected *(0.04 ± 0.02)*
^{133}La	Not Detected *(0.08 ± 0.01)*	Not Detected *(0.11 ± 0.02)*
^{134}La	2341 ± 44 *(1072 ± 133)*	3289 ± 44 *(1454 ± 180)*
^{135}La	127 ± 2 *(117 ± 33)*	183 ± 3 *(165 ± 46)*
^{136}La	224 ± 8 *(217 ± 41)*	312 ± 11 *(297 ± 57)*
Purity [%]		
2h after EOB	99.944 ± 0.002 *(99.892 ± 0.005)*	99.946 ± 0.002 *(99.892 ± 0.005)*

(99.944 ± 0.002)% and (99.946 ± 0.002)%, respectively. These values are in good agreement with the expected yield of 0.057 GBq/μAh (Fig. 28) and a radionuclidic purity of 99.892%. It should be noted that the experimentally determined radionuclidic purity is likely overestimated. In fact, ^{133}La could not be experimentally quantified due to the very low activity produced and to the low intensity of its γ-line (see Table 1). As a consequence, the contribution of ^{133}La to the total activity could not be included in the experimental purity evaluation.

3.4. ^{133}La optimized production

The production cross sections and TTYs of La radioisotopes, calculated from the measured reaction cross sections for an enriched $^{134}BaCO_3$ (isotopic composition reported in Table 2), are shown in Figs. 29 and 30, respectively.

It can be observed that, in this case, the use of an infinitely thick target does not provide any advantage, as the threshold energy for the ^{134}Ba(p,2n)^{133}La reaction is approximately 12.5 MeV. Below this energy, no additional ^{133}La production occurs, while the production

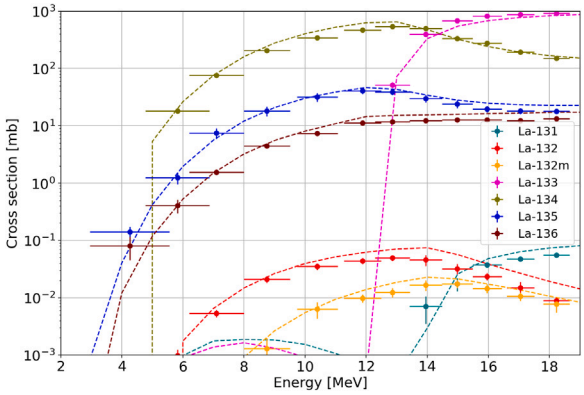

Fig. 29. Production cross sections of La radioisotopes obtained irradiating a 84.2% enriched $^{134}BaCO_3$ target (see Table 2).

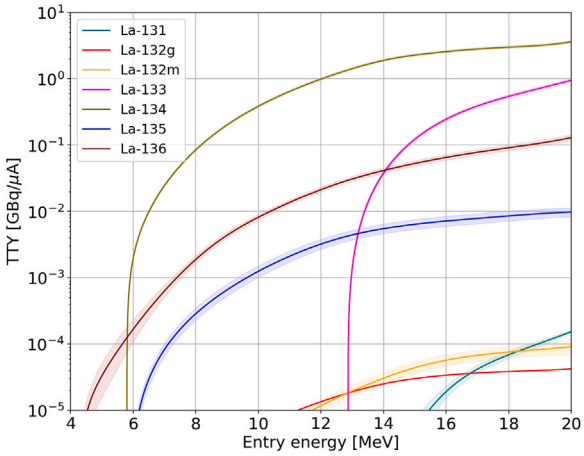

Fig. 30. Thick target yields of La radioisotopes as a function of the proton entry energy for an 84.2% enriched $^{134}BaCO_3$ target. The irradiation time is set to 1 h.

of other La impurities, in particular ^{135}La, increases. Due to its long half-life, ^{135}La cannot be removed from the sample by decay and therefore represents the main impurity of concern. For this reason, the dependence of ^{133}La and ^{135}La yields on target thickness was investigated for an incident proton energy of 18.2 MeV, corresponding to the maximum energy available at the Bern Medical Cyclotron. As shown in Fig. 31, the ratio of ^{135}La to ^{133}La increases sharply for thicknesses above 500 μm. In order to maximize the ^{133}La yield while maintaining an approximately constant ^{135}La/^{133}La ratio, the optimal target thickness was identified in the range 450–500 μm. In this interval, the ^{135}La/^{133}La ratio remains nearly constant, whereas the ^{133}La production yield increases significantly.

Considering an entry energy of 18.2 MeV and a 0.47-mm-thick target, a ^{133}La yield of 0.41 GBq/μA is obtained for 1-h irradiation. Under these conditions, the radionuclidic purity exceeds 99% between 1 and 5 h after EOB (Fig. 32), which corresponds to the time window required for radiochemical processing and transport prior to patient administration.

To further increase the production yield, either a higher incident energy and/or longer irradiation time can be considered. In the latter case, however, particular attention must be paid to the co-production of ^{135}La, whose fraction relative to ^{133}La increases almost linearly with irradiation time (Fig. 33). This results in a progressive reduction of the achievable radionuclidic purity and a shortening of the time interval during which purity exceeds 99% (Fig. 34).

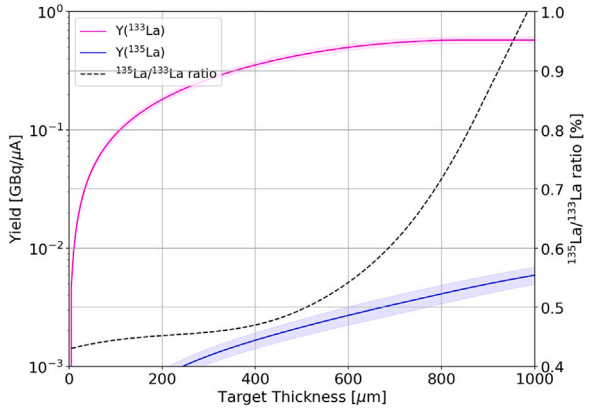

Fig. 31. ^{133}La and ^{135}La yields and the corresponding ^{135}La/^{133}La ratio as a function of target thickness. The incident proton energy is set to 18.2 MeV and the irradiation time is fixed to 1 h.

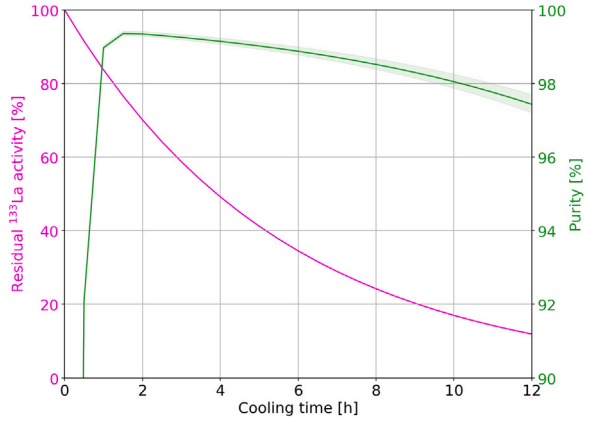

Fig. 32. ^{133}La residual activity and radionuclidic purity as a function of cooling time. The irradiation time is set to 1 h.

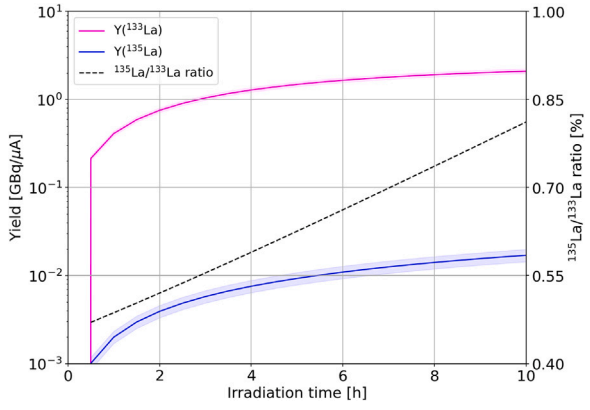

Fig. 33. ^{133}La and ^{135}La yields and corresponding ^{135}La/^{133}La ratio as a function of irradiation time.

Based on these considerations, production tests were performed by irradiating a 0.47-mm-thick enriched $^{134}BaCO_3$ pellet with an 18.2-MeV proton beam. Two irradiations were carried out approximately one month apart, allowing all radionuclides produced during the first test to completely decay.

The incident energy, irradiation parameters, and radionuclide activities measured with the HPGe detector are reported in Table 9. The experimental results were compared with the expected activities

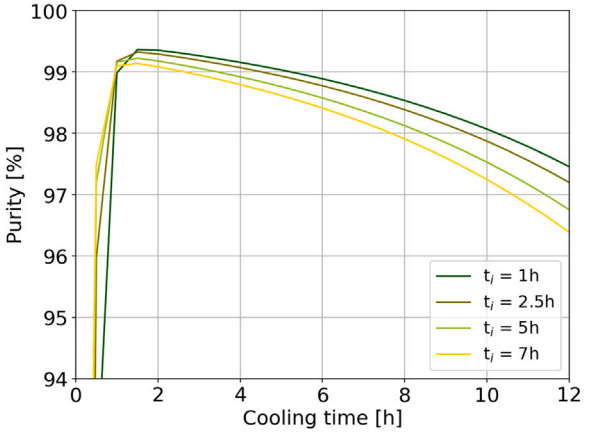

Fig. 34. ^{133}La radionuclidic purity as a function of cooling time for different irradiation times.

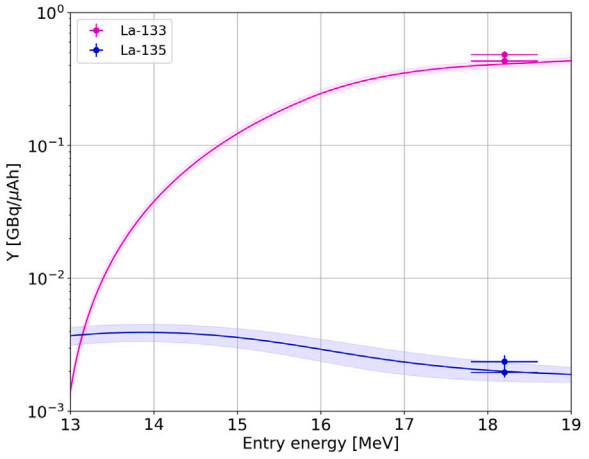

Fig. 35. ^{133}La and ^{135}La yields calculated from the measured cross sections in our irradiation conditions compared with the experimental results.

calculated from the measured cross sections, showing an overall good agreement within uncertainties.

Regarding ^{133}La, the two production tests provided yields of (0.43 ± 0.02) GBq/μAh and (0.48 ± 0.02) GBq/μAh, with radionuclidic purities 2 h after EOB of (99.39 ± 0.04)% and (99.32 ± 0.07)%, respectively. These values are in good agreement with the expected yield of 0.40 GBq/μAh (Fig. 35) and a calculated radionuclidic purity of 99.38%.

4. Conclusion and outlooks

In this work, a comprehensive experimental study of proton-induced nuclear reactions on barium carbonate targets was carried out with the aim of optimizing the production of the medically relevant radionuclides ^{133}La and ^{135}La. Cross sections were measured up to 18 MeV for all reaction contributing to the production of lanthanum radioisotopes, using natural $BaCO_3$ as well as enriched $^{134}BaCO_3$ and $^{135}BaCO_3$ targets. These data significantly extended the existing experimental database, which was found to be incomplete or missing for several reaction channels, and highlighted the importance of high-quality experimental data. On the basis of the measured cross sections, thick target yields and purities were assessed under realistic irradiation conditions. Optimized production routes were identified for both ^{133}La and ^{135}La.

For ^{135}La, irradiation of 93.3% enriched $^{135}BaCO_3$ targets at proton energies below 14 MeV allows the production of this radionuclide with

Table 9
Irradiation parameters and La activities at EOB obtained irradiating a 0.46-mm-thick enriched $^{134}BaCO_3$ pellet. The values in parenthesis are the activity calculations based on the cross-section measurements.

	Test 1	Test 2
E_{in} [MeV]	18.2 ± 0.4	18.2 ± 0.4
t_i [min]	21.2	7.7
I [nA]	5.9	5.6
Activity [kBq]		
^{131}La	0.23 ± 0.09 *(0.17 ± 0.03)*	Not Detected *(0.06 ± 0.01)*
^{132}La	Not Detected *(0.015 ± 0.006)*	Not Detected *(0.005 ± 0.002)*
^{132m}La	Not Detected *(0.09 ± 0.03)*	Not Detected *(0.04 ± 0.01)*
^{133}La	907 ± 7 *(886 ± 110)*	351 ± 3 *(313 ± 39)*
^{134}La	3386 ± 137 *(3326 ± 307)*	2168 ± 36 *(2001 ± 185)*
^{135}La	4.1 ± 0.2 *(4.1 ± 1.3)*	1.7 ± 0.2 *(1.4 ± 0.4)*
^{136}La	177 ± 15 *(169 ± 34)*	92 ± 12 *(87 ± 17)*
Purity [%]		
2h after EOB	99.39 ± 0.04 *(99.38 ± 0.06)*	99.32 ± 0.07 *(99.38 ± 0.06)*

Table 10
Cross-section data of the ^{132}Ba(p,2n)^{131}La nuclear reaction measured from natural $BaCO_3$ targets.

E [MeV]	^{132}Ba(p,n)^{131}La [mb]
4.3 ± 1.3	Not detected
5.8 ± 1.1	Not detected
7.1 ± 0.9	Not detected
8.8 ± 0.8	Not detected
10.4 ± 0.7	Not detected
11.9 ± 0.6	Not detected
12.9 ± 0.6	Not detected
14.0 ± 0.5	80 ± 40
15.0 ± 0.5	198 ± 51
16.0 ± 0.5	425 ± 36
17.1 ± 0.5	538 ± 50
18.2 ± 0.4	625 ± 47

Table 11
Cross-section data of the ^{132}Ba(p,n)^{132cum}La and ^{132}Ba(p,n)^{132m}La nuclear reactions measured from natural $BaCO_3$ targets.

E [MeV]	^{132}Ba(p,n)^{132cum}La [mb]	^{132}Ba(p,n)^{132m}La [mb]
4.3 ± 1.3	Not detected	Not detected
5.8 ± 1.1	11 ± 3	Not detected
7.1 ± 0.9	61 ± 9	Not detected
8.8 ± 0.8	241 ± 31	15 ± 8
10.4 ± 0.7	398 ± 50	72 ± 23
11.9 ± 0.6	497 ± 56	112 ± 18
12.9 ± 0.6	559 ± 59	141 ± 26
14.0 ± 0.5	518 ± 109	189 ± 39
15.0 ± 0.5	366 ± 72	200 ± 32
16.0 ± 0.5	267 ± 38	166 ± 30
17.1 ± 0.5	169 ± 46	120 ± 20
18.2 ± 0.4	101 ± 15	88 ± 25

high yield (0.68 GBq/μA for a 10 h irradiation) and radionuclidic purity exceeding 99.9% after a short cooling time, effectively suppressing short-lived impurities.

For ^{133}La, the use of 84.2% enriched $^{134}BaCO_3$ targets at 18.2 MeV and carefully selected target thickness enables high production yields (0.41 GBq/μA for an irradiation time of 1 h) while maintaining radionuclidic purities above 99% within a clinically relevant time window.

The experimental production tests performed under low-current conditions confirmed the reliability of the calculated yields and purity estimates, demonstrating the feasibility of producing both radionuclides at medical cyclotrons. Overall, the results presented in this work establish optimized and experimentally validated production routes for ^{133}La and ^{135}La, supported by new cross-section data and realistic yield and purity assessments.

Future investigations will address the behavior of $BaCO_3$ targets under high-current irradiation, with cyclotrons and possibly in future with linacs, combining Monte Carlo simulations and dedicated experimental studies to evaluate thermal performance and production scalability. These developments will further consolidate the practical implementation of ^{133}La and ^{135}La for theranostic applications in nuclear medicine.

CRediT authorship contribution statement

Gaia Dellepiane: Writing – review & editing, Writing – original draft, Visualization, Validation, Software, Methodology, Investigation, Formal analysis, Data curation, Conceptualization. **Lars Eggimann:** Writing – review & editing, Methodology, Investigation, Conceptualization. **Alexander Gottstein:** Methodology, Investigation. **Samuel Juillerat:** Methodology, Investigation. **Eva Kasanda:** Methodology, Investigation. **Isidre Mateu:** Writing – review & editing, Methodology, Investigation. **Paola Scampoli:** Writing – review & editing, Conceptualization. **Saverio Braccini:** Writing – review & editing, Supervision, Resources, Project administration, Methodology, Funding acquisition, Conceptualization.

Declaration of competing interest

The authors declare the following financial interests/personal relationships which may be considered as potential competing interests: Saverio Braccini reports financial support was provided by Swiss National Science Foundation. If there are other authors, they declare that they have no known competing financial interests or personal relationships that could have appeared to influence the work reported in this paper.

Acknowledgments

We acknowledge contributions from LHEP engineering and technical staff and from the Interfacial electrochemistry group of DCBP. This research project was partially funded by the Swiss National Science Foundation (SNSF), Switzerland (grants: CRSII5_180352 and IZURZ2_224901).

Appendix 5

See Tables 10–18.

Data availability

Data will be made available on request.

Table 12
Cross-section data of the $^{134}Ba(p,2n)^{133}La$ nuclear reaction measured from natural $BaCO_3$ and enriched $^{134}BaCO_3$ targets.

E [MeV]	$^{134}Ba(p,2n)^{133}La$ (nat. Ba) [mb]	$^{134}Ba(p,2n)^{133}La$ (enr. 134Ba) [mb]
4.3 ± 1.3	Not detected	Not detected
5.8 ± 1.1	Not detected	Not detected
7.1 ± 0.9	Not detected	Not detected
8.8 ± 0.8	Not detected	Not detected
10.4 ± 0.7	Not detected	Not detected
11.9 ± 0.6	Not detected	Not detected
12.9 ± 0.6	70 ± 18	61 ± 7
14.0 ± 0.5	Not detected	470 ± 34
15.0 ± 0.5	776 ± 129	809 ± 52
16.0 ± 0.5	895 ± 88	983 ± 62
17.1 ± 0.5	1083 ± 137	1033 ± 64
18.2 ± 0.4	985 ± 56	1097 ± 66

Table 13
Production cross-section data of ^{134}La measured from natural $BaCO_3$, enriched $^{134}BaCO_3$ and enriched $^{135}BaCO_3$ targets, whose isotopic composition is reported in Table 2.

E [MeV]	nat $Ba(p,x)^{134}La$ [mb]	enr.$^{134}Ba(p,x)^{134}La$ [mb]	enr.$^{135}Ba(p,x)^{134}La$ [mb]
4.3 ± 1.3	Not detected	Not detected	Not detected
5.8 ± 1.1	Not detected	18 ± 1	Not detected
7.1 ± 0.9	2.2 ± 0.4	76 ± 6	Not detected
8.8 ± 0.8	6.1 ± 0.6	206 ± 14	Not detected
10.4 ± 0.7	11 ± 1	346 ± 28	Not detected
11.9 ± 0.6	14 ± 1	469 ± 35	14 ± 1
12.9 ± 0.6	30 ± 2	542 ± 31	152 ± 11
14.0 ± 0.5	39 ± 3	502 ± 39	299 ± 23
15.0 ± 0.5	45 ± 3	334 ± 18	458 ± 25
16.0 ± 0.5	50 ± 4	277 ± 13	639 ± 35
17.1 ± 0.5	51 ± 4	196 ± 15	581 ± 31
18.2 ± 0.4	52 ± 5	151 ± 12	670 ± 36

Table 14
Cross-section data of the $^{134}Ba(p,n)^{134}La$ and $^{135}Ba(p,2n)^{134}La$ nuclear reactions.

E [MeV]	$^{134}Ba(p,n)^{134}La$ [mb]	$^{135}Ba(p,2n)^{134}La$ [mb]
4.3 ± 1.3	Not detected	Not detected
5.8 ± 1.1	21 ± 1	Not detected
7.1 ± 0.9	90 ± 5	Not detected
8.8 ± 0.8	245 ± 11	Not detected
10.4 ± 0.7	411 ± 23	Not detected
11.9 ± 0.6	556 ± 29	13 ± 1
12.9 ± 0.6	629 ± 25	174 ± 11
14.0 ± 0.5	571 ± 32	342 ± 19
15.0 ± 0.5	359 ± 14	504 ± 23
16.0 ± 0.5	280 ± 9	676 ± 30
17.1 ± 0.5	184 ± 11	646 ± 28
18.2 ± 0.4	127 ± 7	721 ± 34

Table 15
Production cross-section data of ^{135}La measured from natural $BaCO_3$ and enriched $^{135}BaCO_3$ targets, whose isotopic composition is reported in Table 2.

E [MeV]	nat $Ba(p,x)^{135}La$ [mb]	enr.$^{135}Ba(p,x)^{135}La$ [mb]
4.3 ± 1.3	Not detected	2.1 ± 0.5
5.8 ± 1.1	1.2 ± 0.4	19 ± 4
7.1 ± 0.9	7 ± 1	114 ± 24
8.8 ± 0.8	21 ± 4	275 ± 54
10.4 ± 0.7	36 ± 7	484 ± 85
11.9 ± 0.6	50 ± 9	597 ± 73
12.9 ± 0.6	62 ± 11	522 ± 63
14.0 ± 0.5	73 ± 17	319 ± 57
15.0 ± 0.5	70 ± 18	218 ± 40
16.0 ± 0.5	66 ± 12	146 ± 25
17.1 ± 0.5	68 ± 11	112 ± 16
18.2 ± 0.4	68 ± 6	104 ± 19

Table 16
Cross-section data of the $^{135}Ba(p,n)^{135}La$ and $^{136}Ba(p,2n)^{135}La$ nuclear reactions.

E [MeV]	$^{135}Ba(p,n)^{135}La$ [mb]	$^{136}Ba(p,2n)^{135}La$ [mb]
4.3 ± 1.3	2.3 ± 0.5	Not detected
5.8 ± 1.1	20 ± 5	Not detected
7.1 ± 0.9	122 ± 25	Not detected
8.8 ± 0.8	295 ± 58	Not detected
10.4 ± 0.7	519 ± 91	Not detected
11.9 ± 0.6	636 ± 76	108 ± 53
12.9 ± 0.6	548 ± 65	331 ± 81
14.0 ± 0.5	320 ± 55	662 ± 166
15.0 ± 0.5	209 ± 36	715 ± 196
16.0 ± 0.5	132 ± 22	734 ± 136
17.1 ± 0.5	93 ± 13	792 ± 125
18.2 ± 0.4	85 ± 19	799 ± 63

Table 17
Production cross-section data of ^{136}La measured from natural $BaCO_3$ and enriched $^{135}BaCO_3$ targets, whose isotopic composition is reported in Table 2.

E [MeV]	nat $Ba(p,x)^{136}La$ [mb]	enr.$^{135}Ba(p,x)^{136}La$ [mb]
4.3 ± 1.3	0.4 ± 0.2	Not detected
5.8 ± 1.1	2.0 ± 0.5	Not detected
7.1 ± 0.9	7.8 ± 0.9	Not detected
8.8 ± 0.8	22 ± 2	7 ± 1
10.4 ± 0.7	36 ± 3	12 ± 1
11.9 ± 0.6	61 ± 5	19 ± 2
12.9 ± 0.6	76 ± 6	14 ± 2
14.0 ± 0.5	88 ± 7	11 ± 2
15.0 ± 0.5	93 ± 7	9 ± 2
16.0 ± 0.5	96 ± 7	9 ± 2
17.1 ± 0.5	93 ± 7	8 ± 2
18.2 ± 0.4	101 ± 7	8 ± 2

Table 18
Cross-section data of the $^{136}Ba(p,n)^{136}La$ and $^{137}Ba(p,2n)^{136}La$ nuclear reactions.

E [MeV]	$^{136}Ba(p,n)^{136}La$ [mb]	$^{137}Ba(p,2n)^{136}La$ [mb]
4.3 ± 1.3	5 ± 2	Not detected
5.8 ± 1.1	26 ± 7	Not detected
7.1 ± 0.9	99 ± 11	Not detected
8.8 ± 0.8	281 ± 23	Not detected
10.4 ± 0.7	465 ± 37	Not detected
11.9 ± 0.6	590 ± 51	133 ± 7
12.9 ± 0.6	359 ± 47	424 ± 20
14.0 ± 0.5	182 ± 63	653 ± 20
15.0 ± 0.5	121 ± 46	746 ± 33
16.0 ± 0.5	93 ± 70	786 ± 15
17.1 ± 0.5	72 ± 57	775 ± 24
18.2 ± 0.4	58 ± 47	856 ± 33

References

Abdelshafy, M.S., Ali, B.M., Elmageed, K.E.A., Nafie, H.O., Hassan, H.E., Al-Abyad, M., 2022. Study of activation cross sections of proton induced reactions on natBa and natCe near their threshold energy regions. Radiochim. Acta 110 (11), 891–901. http://dx.doi.org/10.1515/ract-2022-0048.

Abel, E.P., Clause, H.K., Fonslet, J., Nickles, R.J., Severin, G.W., 2018. Half-lives of ^{132}La and ^{135}La. Phys. Rev. C 97, 034312. http://dx.doi.org/10.1103/PhysRevC.97.034312.

Auger, M., Braccini, S., Carzaniga, T.S., Ereditato, A., Nesteruk, K.P., Scampoli, P., 2016. A detector based on silica fibers for ion beam monitoring in a wide current range. J. Instrum. 11 (03), P03027. http://dx.doi.org/10.1088/1748-0221/11/03/p03027.

Auger, M., Braccini, S., Ereditato, A., Nesteruk, K.P., Scampoli, P., 2015. Low current performance of the Bern medical cyclotron down to the pa range. Meas. Sci. Technol. 26, http://dx.doi.org/10.1088/0957-0233/26/9/094006.

Braccini, S., 2013. The new Bern PET cyclotron, its research beam line, and the development of an innovative beam monitor detector. AIP Conf. Proc. 1525, 144–150. http://dx.doi.org/10.1063/1.4802308.

Braccini, S., Carzaniga, T.S., Dellepiane, G., Grundler, P.V., Scampoli, P., van der Meulen, N.P., Wüthrich, D., 2022. Optimization of ^{68}Ga production at an 18 MeV medical cyclotron with solid targets by means of cross-section measurement of ^{66}Ga, ^{67}Ga and ^{68}Ga. Appl. Radiat. Isot. 110252. http://dx.doi.org/10.1016/j.apradiso.2022.110252.

Buchegger, F., Perillo-Adamer, F., Dupertuis, Y.M., Bischof Delaloye, A., 2006. Auger radiation targeted into DNA: a therapy perspective. Eur. J. Nucl. Med. Mol. Imaging 33, 1352–1363. http://dx.doi.org/10.1007/s00259-006-0187-2.

Carl Roth, A.G., Laborbedarf bei CARL ROTH. URL https://www.carlroth.com/. (Accessed 18 November 2025).

CIAAW, Isotopic composition of the elements. URL https://www.ciaaw.org/isotopic-abundances.htm. (Accessed 2 March 2026).

Dellepiane, G., Aguilar, C.B., Carzaniga, T.S., Casolaro, P., Häffner, P., Scampoli, P., Schmid, M., Braccini, S., 2021. Research on theranostic radioisotope production at the Bern medical cyclotron. IL NUOVO CIMENTO C 44, http://dx.doi.org/10.1393/ncc/i2021-21130-6.

Dellepiane, G., Casolaro, P., Favaretto, C., Grundler, P.V., Mateu, I., Scampoli, P., Talip, Z., van der Meulen, N.P., Braccini, S., 2022. Cross section measurement of terbium radioisotopes for an optimized ^{155}Tb production with an 18 MeV medical PET cyclotron. Appl. Radiat. Isot. 184, 110175. http://dx.doi.org/10.1016/j.apradiso.2022.110175.

Dimitrakopoulou-Strauss, A., Pan, L., Sachpekidis, C., 2023. Long axial field of view LAFOV PET-CT: implementation in static and dynamic oncological studies. Eur. J. Nucl. Med. Mol. Imaging 50 (11), 3354–3362. http://dx.doi.org/10.1007/s00259-023-06222-3.

Durán, M.T., Juget, F., Nedjadi, Y., Bailat, C., Grundler, P.V., Talip, Z., van der Meulen, N.P., Casolaro, P., Dellepiane, G., Braccini, S., 2022. Half-life measurement of ^{44}Sc and ^{44m}Sc. Appl. Radiat. Isot. 190, 110507. http://dx.doi.org/10.1016/j.apradiso.2022.110507.

Fonslet, J., Lee, B.Q., Tran, T.A., Siragusa, M., Jensen, M., Kibédi, T., Stuchbery, A.E., Severin, G.W., 2017. 135La as an Auger-electron emitter for targeted internal radiotherapy. Phys. Med. Biol. 63 (1), 015026. http://dx.doi.org/10.1088/1361-6560/aa9b44.

Forgács, A., Balkay, L., Trón, L., Raics, P., 2014. Excel2Genie: A Microsoft Excel application to improve the flexibility of the Genie-2000 spectroscopic software. Appl. Radiat. Isot. 94, 77–81. http://dx.doi.org/10.1016/j.apradiso.2014.07.005.

IAEA, Live chart of nuclides, available online. URL https://nds.iaea.org/relnsd/vcharthtml/VChartHTML.html. (Accessed 03 March 2026).

International Standard, 2021. Nuclear Instrumentation – Measurement of Activity or Emission Rate of Gamma-Ray Emitting Radionuclides – Calibration and Use of Germanium-Based Spectrometers. IEC 61452:2021.

Juget, F., Durán, M.T., Nedjadi, Y., Talip, Z., Grundler, P.V., Favaretto, C., Casolaro, P., Dellepiane, G., Braccini, S., Bailat, C., van der Meulen, N.P., 2023. Activity measurement of ^{44}Sc and calibration of activity measurement instruments on production sites and clinics. Molecules 28, 1345. http://dx.doi.org/10.3390/molecules28031345.

Khazov, Y., Rodionov, A., Kondev, F.G., 2011. Nuclear data sheets for A=133. Nucl. Data Sheets 112, 855–1113. http://dx.doi.org/10.1016/j.nds.2011.03.001.

Khazov, Y., Rodionov, A., Sakharov, S., Singh, B., 2005. Nuclear data sheets for A=132. Nucl. Data Sheets 104, 497–790. http://dx.doi.org/10.1016/j.nds.2005.03.001.

Khomenko, I.A., Kormazeva, E.S., Novikov, V.I., Aliev, R.A., 2024. Measurement of the cross-sections for the formation of lanthanum radioisotopes in proton induced reactions on Ba-135 nuclei up to 30 MeV. Bull. the Lebedev Phys. Inst. 51, 515–518. http://dx.doi.org/10.3103/S1068335624601869.

Koning, A., Rochman, D., 2012. Modern nuclear data evaluation with the TALYS code system. Nucl. Data Sheets 113, http://dx.doi.org/10.1016/j.nds.2012.11.002, 2841–2934.

Mccutchan, E.A., 2018. Nuclear data sheets for A=136. Nucl. Data Sheets 152, 331–667. http://dx.doi.org/10.1016/j.nds.2018.10.002.

Mirion Technologies, 2022. GENIE 2000 - basic spectroscopy software. URL https://www.mirion.com/products/genie-2000-basic-spectroscopy-software. (Accessed 12 October 2022).

Muminov, V., Mukhammedov, S., Vasidov, A., 1980. Possibilities of proton-activation analysis for determining the content of elements from short-lived radionuclides. Sov. At. Energy 49, 540–544. http://dx.doi.org/10.1007/BF01121617.

Nelson, B.J., Ferguson, S., Wuest, M., Wilson, J., Duke, M.J.M., Richter, S., Soenke-Jans, H., Andersson, J.D., Juengling, F., Wuest, F., 2022. First in vivo and phantom imaging of cyclotron-produced 133La as a theranostic radionuclide for 225Ac and 135La. J. Nucl. Med. 63 (4), 584–590. http://dx.doi.org/10.2967/jnumed.121.262459.

Nelson, B.J.B., Wilson, J., Andersson, J.D., Wuest, F., 2023. Theranostic imaging surrogates for targeted alpha therapy: Progress in production, purification, and applications. Pharmaceuticals 16 (11), http://dx.doi.org/10.3390/ph16111622.

Pedersen, K.S., Deville, C., Søndergaard, U., Jensen, M., Jensen, A.I., 2023. Improved procedures for production and purification of 135La from enriched [135Ba]BaCO3 on a 16.5 MeV cyclotron. Appl. Radiat. Isot. 192, 110612. http://dx.doi.org/10.1016/j.apradiso.2022.110612.

Potkins, D.E., Braccini, S., Nesteruk, K.P., Carzaniga, T.S., Vedda, A., Chiodini, N., Timmermans, J., Melanson, S., Dehnel, M.P., 2017. A low-cost beam profiler based on cerium-doped silica fibers. In: Proceedings of CAARI-16, Physics Procedia. http://dx.doi.org/10.1016/j.phpro.2017.09.061.

Prescher, K., Peiffer, F., Stueck, R., Michel, R., Bodemann, R., Rao, M., Mathew, K., 1991. Thin-target cross sections of proton-induced reactions on barium and solar cosmic ray production rates of xenon-isotopes in lunar surface materials. Nucl. Instrum. Methods Phys. Res. Sect. B 53 (2), 105–121. http://dx.doi.org/10.1016/0168-583X(91)95645-T.

Sandia National Laboratories, InterSpec - spectral radiation analysis software. URL https://sandialabs.github.io/InterSpec/. (Accessed 05 January 2026).

Singh, B., Rodionov, A., Khazov, Y., 2008. Nuclear data sheets for A=135. Nucl. Data Sheets 109, 517–698. http://dx.doi.org/10.1016/j.nds.2008.02.001.

Sonzogni, A.A., 2004. Nuclear data sheets for A=134. Nucl. Data Sheets 103, 1–182. http://dx.doi.org/10.1016/j.nds.2004.11.001.

Tera-Care Foundation, RADIATION diagnostics AND THERAPY FOR all. URL https://tera-care.ch/. (Accessed 05 January 2026).

Trace Science International, Stable isotope supplier. URL https://tracesciences.com/. (Accessed 18 November 2025).

Vasidov, A., Vakilova, G., Muhammedov, S., 1981. The excitation functions of nuclear reactions (p,n) on the isotopes Te, Cs, Ba. Izv. Akad. Nauk. SSSR, Ser. Mat. 3, 92.

Ziegler, J.F., Manoyan, J.M., 2013. The stopping of ions in compounds. Nucl. Instrum. Methods B 35, 215, URL http://www.srim.org.